



**Hydrogen Bonding in the Prism Face of Ice I_h
A Study via Sum Frequency Generation
Vibrational Spectroscopy**

A thesis submitted by

Patrick Joseph Bisson

In partial fulfillment of the requirements for the degree of

Doctor of Philosophy in

Chemistry

TUFTS UNIVERSITY

2013

August

COPYRIGHT © 2013, Patrick Bisson)

ADVISER:

Prof. Mary Jane Shultz

Dedication

To my Mother and Father who supported all my crazy ideas and taught me that dreams can sometimes be realized. I'm sorry I got started so late that they weren't here to see it happen. Still, I hope they would have been proud.

Abstract

The prism face of single crystal ice I_h has been studied using sum frequency vibrational spectroscopy focusing on identification of resonances in the hydrogen-bonded region. Several modes have been observed at about 3400 cm^{-1} ; each mode is both polarization and orientation dependent. The polarization capabilities of sum frequency generation (SFG) are used in conjunction with the crystal orientation to characterize three vibrational modes. These modes are assigned to three-coordinated water molecules in the top-half bilayer having different bonding and orientation motifs.

Such mode identification is only possible with the production and use of single crystal ice of very low defect density and of size appropriate for examination using the SFG technique. Production of single crystal ice is often trivialized in the literature. But in reality, large single crystals are very difficult to produce. Design and construction of an apparatus and protocol that can produce large single crystals of ice truly advances the state of the art. An apparatus utilizing the Bridgeman-Stockbarger method of single crystal growth was designed, constructed and optimized for the growth of ice. This design features a software implemented (LabVIEW) Proportional-Integral-Differential (PID) feedback temperature control algorithm. The temperature at the growth interface was controlled to within $\pm 0.002\text{K}$ even though room temperature variation was ca. $\pm 2\text{K}$.

Since the measurement must occur at cryogenic temperature (ca. 130K), the design and construction of a cell that can enclose and isolate the ice sample from ambient conditions is also of critical importance. An air tight, all glass design was chosen that incorporates two fused IR quartz windows to allow for visible and mid-IR transmittance, an oxygen free copper heat sink and a unique ice mounting scheme. The thermal design

of the heat sink and ice mount are critical for reaching cryogenic temperatures and insuring the ice sample remains attached to the heat sink as the temperature is lowered.

Acknowledgments

First and foremost, I'd like to acknowledge the help and support of my advisor, Prof. Mary Jane Shultz. Professor Shultz' open door policy was very thoroughly exercised by me as I had many questions about many things. I am incredibly thankful to her for many (probably too long) conversations on topics ranging from Chemistry to Optics, from Electromagnetics to Physics, from Psychology to Social sciences, and many other topics I can't list here. Prof. Shultz' breadth of knowledge of such diverse topics truly represents my ideal in a scientist. Probably of even more importance, Prof. Shultz supported me and provided encouragement and guidance for all those scores of machines she asked me to invent and build. Never have so many of my skills and so much of my knowledge been exercised. Similarly, never have I been given such freedom to act. I will always remember my time here as a student of Prof. Shultz.

I would also acknowledge the help and support of those others on my research committee: Professor Jonathan Kenny, Doctor Sergiy Kryatov, and Professor Roger Tobin of the Department Physics and Astronomy. Thank you all for listening quietly and offering insight whenever I offered presentations.

I also want to acknowledge and give special thanks to my former advisor and current representative from an external university on my committee, Professor James Whitten. Prof. Whitten was my boss and advisor when I was studying as an undergraduate at the University of Massachusetts Lowell and working in his laboratory. Prof. Whitten encouraged and supported me in my studies and, like Prof. Shultz, asked me to develop a number of instruments for use in his laboratory. Two of these instruments resulted in published papers.^{1,2} One machine, a continuous flow, moving spectrometer is still in use in his undergraduate teaching laboratory and I am told it is one of the more popular experiments in his course. This is an entirely un-expected result. The

second machine, a low cost Raman spectrometer based on a moderate power (65mW) violet diode laser also found some use in Prof. Whitten's classroom. This prototype was the inspiration for the recent development of a newer, compact design of higher performance. Two of these instruments were built: one for use here at Tufts University in the Shultz laboratory for use in the study of a TiO₂ nanoparticle system, and the other to replace the prototype in Prof. Whitten's teaching laboratory. This design is presented in the Appendix. Nothing pleases me more than to design and build a new and unique machine. I cannot thank Prof. Whitten enough for all his support, encouragement, guidance and friendship.

Also of some importance are my fellow graduate students and lab mates, some of which have already graduated and moved on to greater things. Among these I am particularly thankful to (now) Drs. Irene Li and Henning Groenzin without whose shoulders for me to stand on I would not have accomplished so much. I am also grateful for the friendship and insight of my present lab mates Tuan Vu, Faith Dukes, Rui Liang and especially Jing Wang.

And of course, thanks to the National Science Foundation (Grant CHE-0844986) for funding the ice research.

Table of Contents

Abstract.....	i
Acknowledgments	iii
List of tables.....	viii
List of Figures.....	ix
1 Hydrogen Bonding in the Prism Face of Ice Ih via Sum Frequency Vibrational Spectroscopy.....	1
1.1 Copyright	1
1.2 Introduction.....	1
1.3 Ice Crystal Structure: Face Specification.....	4
1.4 Theory	5
1.5 Experimental.....	9
1.5.1 Optical.....	9
1.5.2 Environmental.....	11
1.5.3 Computer Control	12
1.5.4 Single Crystal Ice Growth.....	14
1.5.5 Selection of crystal plane.....	15
1.5.6 Sample Preparation	16
1.5.7 Rigsby Stage	17
1.5.8 Formvar etching.....	19
1.5.9 Sample mounting	20
1.5.10 Surface Hydrocarbon Determination	23

1.6	SFG Results and Discussion	24
1.6.1	Spectra of basal face	24
1.6.2	Spectra of secondary prism face	26
1.6.3	Discussion and analysis	28
1.7	Conclusion	36
1.8	Future work.....	37
2	Ice Growth Apparatus	38
2.1	Introduction.....	38
2.1.1	Modified Bridgeman-Stockbarger	41
2.1.2	Internal construction	42
2.1.3	Chiller	44
2.2	Modified Bridgeman-Stockbarger computer control	46
2.2.1	PID	46
2.2.2	Software (general).....	48
2.3	Degassing.....	50
3	Ice Growth Habits	52
3.1	Introduction.....	52
3.2	Seed crystal	55
3.3	Temperature stability	55
3.4	Temperature gradient.....	56
4	Summary	58

5	Appendix I	60
5.1	On the simplification of I_{ppp} under certain constraints.....	60
5.2	Ice Crucible Design.....	61
5.3	Ice Cell Design.....	62
5.4	Heat sink design.....	63
5.4.1	Ice carrier	65
5.4.2	Embedding the thermocouple	68
5.5	Raman Spectrometer II	70

List of tables

Table 1.1 – Iconography for Figure 1.2.....	10
Table 1.2 - Summary of results for the 3400 cm ⁻¹ region	28
Table 2.1 - PID Control Coefficients	48
Table 2.2 – GE Model MA100 RTD Calibration Coefficients	48
Table 2.3 - Omega Model PMA PTD Calibration Coefficients.....	49

List of Figures

- Figure 1.1** - Indicating the Bravais-Miller indices of important planes in hexagonal crystals in general..... 5
- Figure 1.2** – Overview of SFG System. Pink: 1064nm; Green: 532nm; Red: Mid IR; Blue: SF; Dotted Red: 10% IR pickoff. Lenses L2 and L3 focus on the sample. Lens L4 performs tuning collimation. Lens L5 matches numeric aperture of monochromator. Short diagonal lines are mirrors. Any electronic cabling is not shown for clarity. See **Table 1.1** for more iconography. 10
- Figure 1.3** - SFG 3.0 User Interface. Scan parameters are set up in the upper left corner, system messages appear in the upper right corner. The raw SFG signal, and IR pulse energy (at the pickoff) are plotted in the lower left corner. The IR normalized SFG is plotted in the lower right corner. A typical scan steps from 2800 – 3600 cm^{-1} by 5 cm^{-1} , and each step acquires 200 SFG pulses. A single spectrum is acquired in about 45 minutes. 13
- Figure 1.4** – A “raw” ice boule after extraction from the glass crucible. The boule is about 25 mm dia. X 130 mm long..... 14
- Figure 1.5** – Home built ice saw. This circular saw replaced a 3-wheel band saw. Changing to a clean-able circular saw proved critical to achieving low hydrocarbon contamination. The 4-degree of freedom ice boule fixture can be seen in the foreground. Pictured here on the workbench at room temperature, the saw and fixture normally reside in the -20 °C freezer..... 15
- Figure 1.6** - a-axis roll determination for prism face samples. The ratio b/a is the longer to the shorter width of a prism face etch pit. See also **Figure 1.1** and **Figure 1.9**..... 16
- Figure 1.7** – Showing the Rigsby stage in a corner of the -20 °C freezer. A light-box at the base casts white light upward through a polarizer (large ring). The polarized light then passes through an ice sample (central, gimbaled ring). After passing through the sample, the (possibly rotated) plane polarized light passed through an analyzer (top ring) that is at right angles to the bottom-most polarizer. The geometry of the apparatus allows for four degrees of freedom..... 18
- Figure 1.8** – Two prism face samples on the Rigsby stage. The perspective is looking down through the instrument, along the central vertical axis. LEFT: a single crystal sample with its c-axis oriented parallel to one of the polarizer axes. Note the c-axis is NOT along the reference flats, but at a small angle in this sample. RIGHT: a polycrystalline sample grown without proper process controls. 18
- Figure 1.9** – Representative Formvar etchings of surfaces on the basal {0001} plane (left) and the secondary prism {2110} plane (right). Based on pit shape, the basal plane is parallel to the surface to within 0.5° and the c-axis of the secondary prism surface (right) is parallel to the surface to within 3.0°. For the

prism face (right), the a -axis “roll” angle off perpendicular is 3.6° . Scale bars are $100\ \mu\text{m}$ 19

Figure 1.10 – Microtome in freezer. The crank handle (lower right) operates the head. A microscope slide and one of the disposable diamond coated blades can be seen on the folded white napkin on top of the machine. Disposable blades are a key part of reducing hydrocarbon contamination. 20

Figure 1.11 – Picture of a freshly sawn prism face, mounted in a carrier (top). The two reference flats, used to help with c -axis determination can be seen on the ice. The fixture used to grip the carrier and affix it to the microtome head is also shown (bottom). A portion of one of the disposable microtome blades can be seen (extreme top). 21

Figure 1.12 – An opened ice cell, at room temperature, on the workbench. The bottom half of the cell (glass) rests on a modified optical shelf kinematic stage and mounting plate. This provides fine pitch/roll control over the ice surface. A freshly made carrier is affixed to the top of the heat sink which extends out the bottom of the cell. The heat-sink flutes, critical for achieving low temperature operation (see Section 5.4), can be seen at the bottom. Two side ports on the glass bottom can be seen. One port is not in use, the other allows passage of a thermocouple to measure ice surface temperature. 22

Figure 1.13 – Line drawing of ice sample within a closed glass cell. The body of the glass cell is omitted for clarity. The sample is mounted in a copper carrier, clamped to the top a copper heat sink that extends downward and is immersed in liquid nitrogen. The fused quartz windows are oriented roughly perpendicular to the beams. The ice sample (hatched field) is 8mm thick x 25mm dia. A type T thermocouple is imbedded in the surface of the ice about 1mm deep. The Vis and IR beams are at 50° and 60° angle of incidence, the SF beam is ca. 52° . Typical ice surface temperature is -165°C 23

Figure 1.14 - Verifying low CH contamination. Both measurements are under similar experimental conditions (except temperature). This plot shows the $2800 - 3000\ \text{cm}^{-1}$ band of a typical *ssp*, basal face ice spectrum (red, squares) as compared to a $0.5x$ acetonitrile concentration at the surface (black, triangles). The upward sweep for the ice data (at the blue end) is the skirt of the $3100\ \text{cm}^{-1}$ peak which exceeds 1.56 in this data set. 24

Figure 1.15 - The basal $\{0001\}$ face of ice in *ssp* (left) and *ppp* (right) polarization. Note that the visible and IR intensities are the same for each spectrum, thus the surface produces a much weaker *ppp* than *ssp* spectrum. The $3400\ \text{cm}^{-1}$ feature (actual $3385\ \text{cm}^{-1}$) is visible in the *ppp* spectrum, but not in the *ssp* spectrum. The amplitude of the *ssp* spectrum is ca. 6.8 times that of the *ppp* spectrum at $3100\ \text{cm}^{-1}$ 25

Figure 1.16 – A prism face, p -oriented, using *ssp* and *ppp* polarization combinations. Left: the two spectra showing relative amplitudes. Right: expanded ordinate-axis highlighting the $3435\ \text{cm}^{-1}$ feature and the different modes observed with polarization. 26

-
- Figure 1.17** – A prism face, *s*-oriented, using *ssp* and *ppp* polarization combinations. Left: the two spectra showing relative amplitudes. Right: expanded ordinate-axis highlighting the reverse sense relationship with polarization and the redder frequency compared to the *p*-oriented surface. 27
- Figure 1.18** - View of the hexagonal ice structure of the basal face at the surface showing the “chair” water structure of the bilayers and bonding between two basal plane bilayers (stitching bonds). Top-half bilayer water molecules (starred) *may* have double donor OH bonds to the lower 4-coordinate molecules in the lower half of the top bilayer. Molecules with this bonding motif contribute to the 3400 cm^{-1} feature. Note that some, but *not all* of these (*) molecules are double donors. Some others but *not all* are single donors, giving rise to the *d*-OH bond. 31
- Figure 1.19** - Schematic of the secondary prism face explicitly showing the three bonding motifs of double-donor surface molecules: (1) double donor to four-coordinate water, (2) double donor with one coordination to a three-coordinate, double-donor molecule and one to a four-coordinate water molecule, (3) double donor with one coordination to a three-coordinate, single-donor molecule and one to a four-coordinate water molecule. Remaining structure is a schematic of the oxygen lattice. The *c* axis lies along the surface dimer bonds; the *a*-axis perpendicular to the surface. 32
- Figure 1.20** - Two configurations for the secondary prism face dimer: (A) the single-donor hydrogen bonds to a double-donor dimer partner (B) the single-donor hydrogen bonds to a single-donor, *d*-OH partner. Both the vibrational frequency and the polarizability of the single donor are altered by its dimer partner. Arrow indicates subject molecule. Upper right: electrostatic potential map. 34
- Figure 2.1** – Diagram of inner structure of modified Bridgeman-Stockbarger apparatus. The outer bath sets the low temperature at $-3\text{ }^{\circ}\text{C}$; the counter heater sets the $0\text{ }^{\circ}\text{C}$ surface. The $0\text{ }^{\circ}\text{C}$ surface is “pinned” within the hole of the shelf by software control. The counter heater establishes a temperature gradient as shown on the left. 39
- Figure 2.2** – Picture of top of ice growth apparatus showing drive system and an ice crucible. The ice growth process is mid-way in this photograph. 40
- Figure 2.3** – Block diagram of ice growth apparatus. A desktop PC communicates with several DMMs using RS-232 and IEEE-488 protocols. Two DMMs read the resistance of an RTD or a PTD and convert that to temperature. Two DMMs read the voltage and current applied to the heating element inside the apparatus. The shelf temperature (RTD) is used as feedback to the PID control algorithm. Control is established by commanding the B&K Precision Model 9130 programmable power supply to a new voltage. 41
- Figure 2.4** – The fully insulated Modified Bridgeman-Stockbarger apparatus sits on a 3-foot square piece of granite, floating on three air pillars for vibration isolation. Supply and return hoses (5/8” ID) circulate 70%wt ethylene/glycol at $-3\text{ }^{\circ}\text{C}$ and at nearly 23 L/min. The drive system and a mounted crucible can be seen at the top. 42

-
- Figure 2.5** – Showing the internal structure of the apparatus. The counter heater is the aluminum tube wrapped with NiCr wire. The shelf with its hole and RTD can be seen at lower left. The crucible clamp and drive system can be seen in upper right. 43
- Figure 2.6** – Picture of the Thermo/NESLAB RTE 740 chiller. The coolant supply and return hoses (black, insulated) can be seen at the rear. The chiller specific electronic control (a PID) is seen mounted on top of the machine. The chiller set-point is $-3.3\text{ }^{\circ}\text{C}$ 45
- Figure 2.7** – The PID algorithm as applied to the ice growing process. The measured temperature $y(t)$ (“output” of the process) is fed back negatively to the input. It is summed against the setpoint temperature $r(t)$ to generate the error signal, $e(t)$. The error signal, $e(t)$, is processed in three ways: 1) the “present” 2) the “history” or the “past”, and 3) the “future” or “predictive”. These three generated signals are then summed and used to derive a new control signal, $u(t)$, to drive the process (shelf temperature) closer to the setpoint. 46
- Figure 2.8** – Ice Machine Temperature Controller Software user interface. The desired shelf temperature setpoint (normally $-1\text{ }^{\circ}\text{C}$) is adjusted in the upper left. If a log file name is provided, the “Logging” button is enabled and the logging function may be started. The “Run/Stop” button enables the temperature control function. The counter heater Voltage/Amperage/Power is indicated along the right hand side. A strip chart indicates the recent history of shelf temperature as compared to setpoint along the bottom of the interface. 50
- Figure 2.9** – Water degassing vacuum line. The ice crucible is connected to the hose with the adaptor at upper right. The bottom of the crucible extends into the glass Dewar (lower right) filled with ice/water. A water trap can be seen at lower center held within the stainless steel Dewar filled with LN2. The mechanical vacuum pump is seen at bottom left of center..... 51
- Figure 3.1** - A double domain boule viewed end-on in the Rigsby stage. This was a case where both c-axes are nearly perpendicular to the domain wall, and also perpendicular to the boule axis. The long optical path (a full 10 cm) makes this test quite sensitive to c-axis orientation. Only a few degrees difference in orientation between the two domains can show one ‘extinct’ and the other to be ‘bright’ 53
- Figure 3.2** - Feathering in a boule. Left: Viewing a boule end-on in the Rigsby stage, the “feathers” form multiple, parallel planes. Right: Viewing (a different boule) side-on. This type of flaw was completely eliminated after positive temperature control was implemented. 56
- Figure 3.3** - A secondary domain. This is a picture of the bottom end of the crucible, freshly out of the growth apparatus, viewed in the Rigsby stage. The polycrystalline seed can be seen in the capillary (upper left). The primary domain of the boule is oriented so that it appears ‘extinct’ (dark). The secondary domain has an odd orientation and so appears ‘bright’. It is clear that the secondary domain has nucleated along the inside surface of the glass crucible and is not connected with the primary seed in the capillary..... 57

-
- Figure 5.1** - Ice Crucible Design. In use, the crucible is filled to 7” water depth. The crucible is clamped into the drive system at the reference line near the top. Each crucible is labeled for tracking purposes. The neck, capillary, and seed bulb play a key role in the domain selection process. 62
- Figure 5.2** - Assembled Cell on the Bench. The perspective is looking at the “output” window. The flat clamping ring and three screws with wing-nuts compress the cap, O-rings, and cup together to make a seal. The cap has been wrapped with one layer of aluminum foil to improve thermal performance. A sample of ice can be seen inside the cell. 63
- Figure 5.3** – The fluted heat sink partially immersed in the LN2. Here, the copper is fully wetted and there is no Leidenfrost vapor barrier. 65
- Figure 5.4** - Linear expansion of Cu vs. Ice. The greatest difference, and therefore the greatest induced strain, occurs at the warmest temperatures. Experimentally, cracking occurs at about -50 °C. 66
- Figure 5.5** - Ice in a carrier, on the pedestal on the bench. The fused quartz top has been removed to allow this photograph. This is a prism face sample. The thermocouple, used to measure ice surface temperatures, can be seen imbedded in the top surface. 67
- Figure 5.6** - Two carriers being fabricated. The thin 0.002” copper foil is soldered to the carrier body (ring). Afterwards, the excess is trimmed off and the completed carrier is cleaned with a sequence of organic solvents (hexanes, acetone, methanol) to remove flux residues. Following this, the carrier is slightly etched in 0.1M HNO₃ to remove copper oxides. 68
- Figure 5.7** – A partly constructed Raman Spectrometer II. The laser driver/module has been removed (upper left). The excitation arm is upper left to center. The scattering arm is center to upper right. The blue fiber optic couples the scattered Raman light to the USB-4000 (top center). 71
- Figure 5.8** – Operational check of Raman Spectrometer II. The laser is operating a little redder than usual. The diode was later replaced with one operating closer to 405nm for a better match to the 405nm notch filter. This instrument is about twice as sensitive as the original design. 72

1 Hydrogen Bonding in the Prism Face of Ice Ih via Sum Frequency Vibrational Spectroscopy

1.1 Copyright

Reproduced in part with permission from: Bisson, P. J.; Shultz, M. J. Hydrogen Bonding in the Prism Face of Ice Ih via Sum Frequency Vibrational Spectroscopy. *J. Phys. Chem. A* **2013**. Copyright 2013 American Chemical Society.

1.2 Introduction

Water and aqueous solutions play important roles in numerous environmental, biological, and geological systems. In many of these settings, key interactions occur at the surface. Not surprisingly, there is a large body of work reporting experimental probes of the aqueous interface.³⁻¹⁷ Like most properties of water,^{18,19} hydrogen bonding plays a pivotal role in determining the surface properties. Since the OH stretch of water is very sensitive to the hydrogen-bonding environment, vibrational spectroscopy would seem to be an ideal probe not only for interactions at the aqueous solution interface, but also for alteration in the hydrogen-bond structure of water due to these interactions. Water, however, is notoriously opaque to infrared radiation.

One approach for circumventing the opacity issue is to use reflection-absorption infrared spectroscopy.²⁰⁻²² Reflection-absorption spectra are biased toward the surface precisely due to the strong absorption cross section of water. Another approach is to use a nonlinear spectroscopy that depends on breaking the macroscopic center-of-inversion that occurs right at the interface. The technique called sum frequency generation (SFG) is

both a nonlinear and a vibrational spectroscopy. SFG would thus seem an ideal probe for answering questions about interactions at the aqueous interface.

SFG, however, does not solve one major issue with diagnosing water structures at aqueous interfaces: the hydrogen bonding region of water (ca. $2900\text{ cm}^{-1} - 3800\text{ cm}^{-1}$) is broad, covering most of the mid-infrared region. The breadth suggests that the spectrum consists of multiple, closely spaced and overlapping modes. There are several approaches to deconvolute the individual resonances to identify hydrogen-bonded motifs that are altered with interaction: put salts or ions in the water and monitor water's response,^{13,17,23-26} use isotopic dilution,^{15,27-31} trace energy transfer in a spectral diffusion experiment,³²⁻³⁵ or decompose the broad spectrum into its components by fitting the profile.^{13,15} As discussed below, the nonlinear nature of SFG requires additional information to make the deconvolution unique. Thus, in recent years, SFG has been augmented with what are called phase measurements³⁶⁻³⁸ that are, in effect, measurements of the complex (i.e.: real and imaginary) SFG spectrum. Results of the complex SFG measurements indicate that the resonances are indeed broad.

Broad resonances result because in the liquid state, thermal motion and short lifetimes act together to broaden resonances. The reported work thus takes an approach that addresses these two problems: thermal energy is limited by studying cryogenic ice and because the water is in the solid phase, hydrogen-bond lifetimes are extended thereby narrowing resonances. The number of orientations is reduced by using well-oriented, single-crystal samples. The result is fewer spectral lines and the ones that are present are narrower and more intense. The reported work includes three additional dimensions to identify resonances: it probes both the prism and the basal face of ice combining crystal orientation with the inherent polarization dependence of SFG. The result is assignment of three resonances, augmenting the free-OH³⁹ and bilayer stitching bonds⁴⁰⁻⁴² previously identified.

Most previous studies of ice have focused on the basal or $\{0001\}$ face of ice.³⁹⁻⁴⁷ The prism face seems to have been relatively neglected. This is unfortunate because the prism face has a number of interesting attributes. Briefly, ice is anisotropic on several levels: growth, surface energy, optical (bulk), thermal, and mechanical to name a few.^{18,19,48,49} Relevant to this work, the anisotropy extends to the optical characteristics of the surface itself. For example, a prism face can be oriented either with the optical axis in the plane of incidence (the plane formed by the probe beams and the surface normal), called p oriented, or perpendicular to it, called s oriented. This optical anisotropy affects the content, or texture, of the vibrational spectrum. Crystal orientation provides additional information leading to a richer understanding of the structure and bonding at the surface.

This research focusses on the secondary prism face, $\{\bar{2}110\}$ and comparing it to the basal face $\{0001\}$. Although both primary and secondary prism faces are common in nature (easily observed as the edges of nearly any snowflake), the secondary prism face is chosen for several reasons: 1) based on the principle that the higher energy faces are both least exposed and most reactive⁵⁰⁻⁵² the secondary prism face is likely more chemically active than the primary prism face, 2) during slow growth from the melt from polycrystalline seeds, we most frequently observe the secondary prism face at the ice/water interface, and 3) the secondary prism face presents a unique dimer motif. This observation of a preferred a -axis orientation is based on the growth of nearly one hundred boules. The observed ice growth habit is the subject of Section 3.

This section presents the results of a study of the secondary prism face as compared to the basal face via SFG. This section contains a brief discussion of crystal orientation conventions and of the applicable portions of SFG theory including those relevant to polarization. This is followed by experimental details including optical setup, growth apparatus, and crystal preparation. The Results section presents data for the basal and prism faces including the polarization dependence. The discussion section uses the

polarization and crystal orientation information from the SFG theory section to interpret the data in the results section and arrive at an assignment for three vibrational resonances in the hydrogen-bonded region.

1.3 Ice Crystal Structure: Face Specification

The stable form of ice at atmospheric pressure is hexagonal ice (I_h). A schematic of the hexagonal prism is shown in **Figure 1.1**, which indicates the Bravais-Miller indices. This work focuses on hydrogen bonding in the $\{\bar{2}110\}$ face, called the secondary prism face (**Figure 1.19**), comparing spectra to those from the basal face (**Figure 1.18**).

Ice, although crystalline, contains relatively high residual entropy. That is, the oxygen lattice forms a regular array, but the protons form a disordered structure satisfying the so-called Bernal-Fowler⁵³ ice rules (often misattributed to Pauling⁵⁴): (a) Every oxygen atom is four coordinate. (b) Two oxygen coordinations are covalent bonds with hydrogen, and two are hydrogen bonds to neighboring oxygen atoms. (c) Exactly one proton is located between any pair of oxygen atoms. This bonding is disrupted at the surface.

An ideal lattice has perpendicular dangling valences on the basal face and angled dangling valences on prism faces. Due to the local tetrahedral structure of water, the basal face has three-fold rotational symmetry while the prism faces have only two-fold rotational symmetry. As indicated in the Theory section, these characteristic rotational symmetries result in different potential polarizations for the surface hyperpolarizabilities.

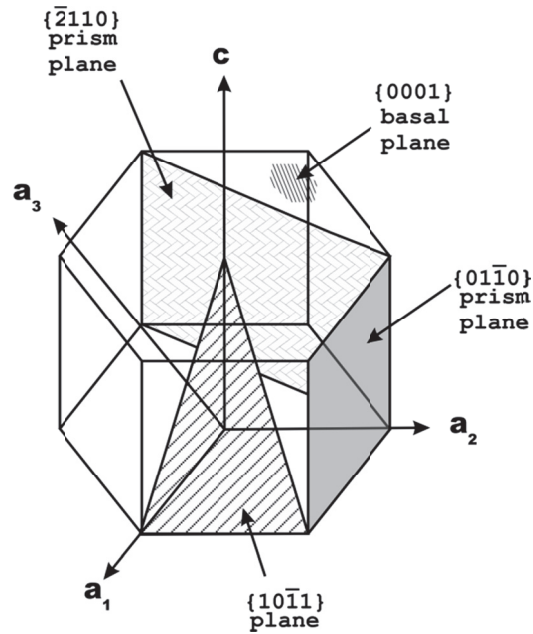


Figure 1.1 - Indicating the Bravais-Miller indices of important planes in hexagonal crystals in general.

1.4 Theory

Sum Frequency Generation (SFG) is a nonlinear optical technique for obtaining a vibrational spectrum of molecules at an interface. The theory of SFG has been well described so only the details needed here are discussed. For a detailed explanation of the theory and practice of SFG, see references⁵⁵⁻⁶⁰ among others.

The SFG signal is generated by combining a visible and an infrared pulse at the interface. The intensity of the generated signal is related to the hyperpolarizability, the visible and infrared excitation fields, and the spatial average of the contributing resonances.⁶¹⁻⁶³

$$I(\omega) = \frac{32\pi^3\omega^2\sec\eta_{SF}^2}{c^3n_1(\omega_{SF})n_1(\omega_1)n_1(\omega_2)} \left| \vec{E}(\omega_{SF}) \cdot \tilde{\chi}^{(2)} : \vec{E}(\omega_{VIS})\vec{E}(\omega_{IR}) \right|^2 \quad (1.1)$$

where: η is the sum frequency signal incident angle (from the surface normal), \vec{E} is the electric field vector for the specified beam, $n_i(\omega_j)$ is the index of refraction in medium i at frequency ω_j , $\tilde{\chi}^{(2)}$ is the hyperpolarizability tensor of the surface, and c is

the speed of light. Note that this expression contains the polarization of the generated sum frequency signal via $\tilde{E}(\omega_{SF})$, dependence on the polarization of the visible $\tilde{E}(\omega_{VIS})$, and IR beams $\tilde{E}(\omega_{IR})$, and the net orientation of the molecules at the surface via $\chi^{(2)}$. In the reported experiment, the visible and IR beams are co-planar defining the plane of incidence via the surface normal and the direction of propagation.

This study uses the polarization and resonance orientation dependence of the hyper-polarizability tensor, so these are discussed briefly. The hyperpolarizability tensor is a property of the surface; its resonance properties encapsulate the vibrational spectrum as follows. Individual vibrational resonances are well described by a complex Lorentzian; the spectrum of multiple modes is described by the sum of the complex amplitudes and a possible non-resonant component:

$$\chi_{lmn}^{(2)} \propto \chi_{lmn,NR} + \chi_{lmn,R} = \chi_{lmn,NR} + \sum_q \frac{A_{lmn,q}}{(\omega - \omega_q) + i\Gamma_q} \quad (1.2)$$

where: $\chi_{lmn}^{(2)}$ represents one element of the non-linear hyper-polarizability tensor; A_q , ω_q and Γ_q represent the amplitude, frequency, and damping constant of the q th resonance. Because $\chi^{(2)}$ is complex, the sum of amplitudes contained in Eq. (1.1.2) results in interferences among the resonances. This is unlike a simple, linear infrared absorption where the mode intensities add. Molecular orientation with respect to the surface enters via spatial averaging of the molecular hyperpolarizabilities, $\beta_{\alpha\beta\gamma}$, to produce the resonant surface hyperpolarizability, $A_{q,lmn}$:

$$A_{q,lmn} = N_s \sum_{lmn} \langle lmn | \alpha\beta\gamma \rangle \beta_{q,lmn} \quad (1.3)$$

where: N_s is the number of scatterers and $\langle | \rangle$ denotes spatial averaging over the molecular orientation distribution and rotation of the molecular reference frame to the surface reference frame, and $\beta_{q,lmn}$ is:

$$\beta_{q,lmn} = \frac{\partial \alpha_{q,lm}}{\partial Q_q} \frac{\partial \mu_{q,n}}{\partial Q_q} \quad (1.4)$$

where: α and μ are the Raman tensor and dipole vector respectively.

Thus the $A_{lmn,q}$ of Eq. (1.1.2) are elements of a tensor that reflects variation of the amplitude of each mode with orientation and polarization. This research uses sensitivity to polarization and orientation to determine mode assignments.

In general the observed intensity i.e.: Eq. (1.1) involves 27 elements of the third order $\chi^{(2)}$ tensor. In many cases, spatial averaging significantly reduces that number. Specifically, for an isotropic surface (e.g. liquids), or a surface that has a mirror plane along the plane of incidence (e.g. basal and prism faces of ice), *s*-polarized visible, and *p*-polarized IR light produce an *s*-polarized sum frequency signal.^{55,62} In this case, Eq. (1.1) reduces to:

$$I_{ssp} \propto |L_Y \chi_{YYZ} K_Y^{vis} K_Z^{IR} e_{vis}^s e_{IR}^p|^2 \quad (1.5)$$

where: I_{ssp} refers to the generated sum frequency signal, L and K are the nonlinear and linear optical factors respectively,⁵⁵ e refers to the component of the electric field in the specified *s* or *p* direction, and χ_{YYZ} refers to the *YYZ*-th element of the $\chi^{(2)}$ tensor. The surface coordinate system consists of a vertical *Z* axis, coincident with the surface normal (+*z*-axis), the +*X*-axis that lies in the input plane, pointing along the direction of propagation, and the +*Y*-axis defined by the right-hand-rule. Thus, the plane of incidence is the *X-Z* plane. In general, with *p*-polarized visible and *p*-polarized IR light, the sum frequency intensity depends on four hyperpolarizability elements: χ_{XXZ} , χ_{XZX} , χ_{ZXX} , and χ_{ZZZ} . With the additional constraint that the visible and IR beams are nearly co-linear (as in the present configuration) Eq. (1.1) simplifies⁶⁴ (See also Appendix I for details):

$$I_{ppp} \propto \left| \left[\cos \eta_{r,SF} \chi_{XXZ} L_X K_X^{vis} + \sin \eta_{r,SF} \chi_{ZZZ} L_Z K_Z^{vis} \right] K_Z^{IR} e_{vis}^p e_{IR}^p \right|^2 \quad (1.6)$$

The sign of the product of optical factors $L_X K_X^{vis}$ is opposite to that of the $L_Z K_Z^{vis}$ optical factors due to reflection at the interface.⁵⁵ Note further that the intensity is the square of the complex sum, not the sum of the squares. I_{ppp} is thus the result of *interference* between χ_{XXZ} and χ_{ZZZ} . Because of this interference, the *ppp* signal is often less intense than the *ssp* signal.

For a surface with three-fold or higher rotational symmetry, *XX* and *YY* polarizabilities in the surface coordinate system are equivalent. If such a surface is oriented so that the input plane is also a surface mirror plane, then there are only four unique non-zero elements of the hyperpolarizability tensor: $\chi_{XXZ} = \chi_{YYZ}$, $\chi_{XZX} = \chi_{YZY}$, $\chi_{ZXX} = \chi_{ZYY}$; and χ_{ZZZ} . This case applies to the basal face of ice. The prism face has richer features because the Z axis is has a two-fold rotational symmetry. As a result, the equivalences indicated above are removed and there remain seven unique non-zero elements. This work exploits this nonequivalence, along with the ability to rotate the surface, to associate resonances with surface bonding motifs.

SFG probes the hyperpolarizability orientation. As indicated in Eq. (1.1.6), the *ppp* intensity results from interference between χ_{XXZ} and χ_{ZZZ} where the *XYZ* coordinates refer to the laboratory coordinate system. In terms of the surface reference frame, χ_{xxz} is the tangential and χ_{zzz} is the longitudinal hyperpolarizability. Note that correspondence between the laboratory and surface coordinate systems is $x \rightarrow X$, $y \rightarrow Y$, $z \rightarrow Z$ for *p*-oriented prism face, but is $y \rightarrow X$, $x \rightarrow Y$, $z \rightarrow Z$ for *s*-oriented. Due to the two-fold rotational symmetry, the prism face of ice presents the potential to distinguish between the tangential and longitudinal polarizability along the *c* axis and that perpendicular to it. This work uses this potential to deduce spectral assignments.

1.5 Experimental

1.5.1 Optical

The optical setup has been described in some detail elsewhere.⁴⁰ A top-level diagram of the optical bench is provided in **Figure 1.2**. The “instrument” consists of an Nd:YAG laser system (EKSPLA PL-2143A/20) producing 30 mJ per 25 ps pulse at 1064 nm wavelength at 20 Hz PRF. This source radiation was fed into an OPG/OPA (LaserVision, Inc.) to produce coherent, tunable mid-IR radiation in the range of 2000 cm^{-1} to 4000 cm^{-1} and visible laser radiation wavelength fixed at 532 nm wavelength. Frequency calibration of the OPG/OPA was accomplished by using three different thin-film calibration standards: acetonitrile/water, polystyrene and water/ CCl_4 that span the tuning range. The position of selected peaks in the IR absorption spectrum of these references was correlated with measurements of the same standards using a Nicolet Magna System 760 FTIR spectrometer.

The Laser, OPG/OPA, and all optics were mounted on a TMC (Technical Manufacturing Corporation, Peabody MA) optical table suspended on six air pillars for vibration isolation. Most of the electronics, including the desktop PCs and shared display were positioned on a shelf suspended from the ceiling to prevent coupling vibrations from fans on to the table.

Visible laser beam spot diameter on the surface was ca. 1.2 mm; IR laser beam spot diameter was ca. 0.5 mm on the surface. The visible beam pulse energy was 100 $\mu\text{J}/\text{pulse}$ at the surface. The IR beam pulse energy was 22 $\mu\text{J}/\text{pulse}$ at the surface. Input angles were 50° (visible) and 60° (IR). This combination of beam energies and spot sizes produced an approximately balanced visible vs. IR beam energy density at the surface. Energy densities were carefully managed and subsequently verified to produce no detectable spectral change over time.

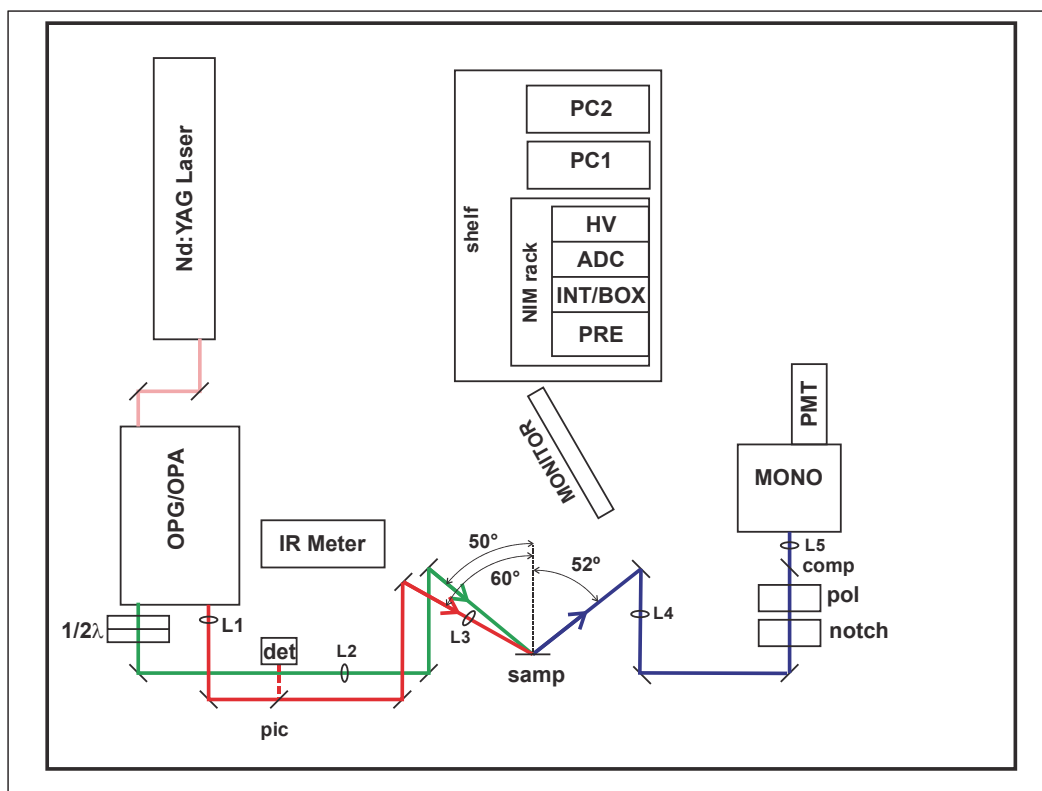


Figure 1.2 – Overview of SFG System. Pink: 1064nm; Green: 532nm; Red: Mid IR; Blue: SF; Dotted Red: 10% IR pickoff. Lenses L2 and L3 focus on the sample. Lens L4 performs tuning collimation. Lens L5 matches numeric aperture of monochromator. Short diagonal lines are mirrors. Any electronic cabling is not shown for clarity. See **Table 1.1** for more iconography.

Table 1.1 – Iconography for Figure 1.2	
Nd:YAG Laser	EKSPLA PL-4320A
OPG/OPA	LaserVision Custom Built 532nm & mid IR tunable
$1/2\lambda$	1" dia x $\frac{1}{2}$ wave plate
IR Meter	Moletron EnergyMax EM-500 with RS-232
det	Moletron J8LP pyro electric IR detector
pic	50mm dia x 1mm thick CaF_2 window, 10% IR pickoff
L1	1" dia x 300mm FL CaF_2 collimation lens (IR)
L2	1" dia x 1000mm FL AR coated Vis objective lens
L3	1" dia x 250mm FL CaF_2 IR objective lens
L4	1" dia x 750mm FL AR coated SF tuning collimator

L5	1" dia x 200mm FL AR coated NA matching lens
samp	Sample surface
notch	Kaiser holographic 532nm notch filter
pol	Karl-Lambrecht 10mm clear aperture Glan-Thompson polarizing prism
comp	Glass polarization compensator
mono	Oriel CS260 monochromator with 600 μ m slit, 1200 line/mm grating
PMT	Hamamatsu R4220p photo multiplier tube
PC1, PC2, monitor	Home built desktop computers and shared monitor
PRE	Stanford Research SR240A low noise preamplifier
INT/BOX	Stanford Research SR250 Integrator/boxcar averager
ADC	Stanford Research SR245 analog/digital converter with RS232 interface
HV	ORTEC 556 adjustable 3kV high voltage power supply
NIM rack	Stanford Research NIM rack

1.5.2 Environmental

Once an ice sample is on the optical bench, a measurement sequence can extend to beyond 8 hours. Therefore, of some importance is the local environmental control to establish long term stability of the system. The entire setup, and a second identical setup, is located within a small ca. 300 ft² facility, or room. The room was specially built to isolate it from external changes in temperature, reduce exchange of atmosphere with the external environment, and to provide a reduced humidity atmosphere. The walls and ceiling incorporate 6 mil thick polyethylene sheets and all doors are gasketed to prevent unmanaged exchange of air with the outside. The facility incorporates a locally designed, totally independent, dedicated air conditioning system specially designed to provide

temperature stability of +/- 0.5 °C. Relative humidity is controlled via a Munters Inc. EC-150 de-humidifier to less than 20%.

1.5.3 Computer Control

The OPG/OPA and various support instruments were controlled by home built operating software (SFG 3.0) designed for the purpose. Briefly, SFG 3.0 is the third generation of a series of custom operating system software for SFG instruments. Written in LabVIEW 8.51, this latest version incorporates a multi-threaded architecture with a message based inter-thread communication system. This architecture leverages the multi-core architecture of the Intel Core-2 Duo CPU which supports true multi-thread execution concurrency. For each instrument controlled by the software, a single thread manages communication and control via an RS-232 interface. A supervisor thread organizes and choreographs a particular SFG measurement based on user preferences. The user interface also operates in a separate thread in order to maintain responsiveness.

The LaserVision OPG/OPA is directly controlled by a separate, dedicated PC. However, the OPG/OPA controller PC communicates with the PC running the SFG 3.0 software via an RS-232 interface. The SFG 3.0 software issues tuning commands and receives actual tuning values to and from the OPG/OPA controller PC. In operation, the OPG/OPA is step tuned rather than velocity tuned. That is to say, the OPG/OPA is commanded to go to a particular wavenumber and then stop. SFG 3.0 is optimized (table lookup) to minimize the tuning time between steps. This step tuning strategy is necessary because it can take several seconds to acquire hundreds of laser flashes necessary for averaging purposes.

The SFG 3.0 software also pulls digital data off the Stanford Research SR245 analog/digital converter. This device digitizes the SF optical pulse integrated by the SR250 integrator/averager. The SR245 is a multi-channel device and the IR pulse energy

detected at the IR pickoff (an analog voltage signal) is also converted. Within SFG 3.0 a dedicated thread pulls these data in real time (i.e.: in between laser flashes) off the SR245.

The raw SF and IR data are processed during idle time by another dedicated thread within SFG 3.0. The processed data are the SF pulse amplitude normalized to the IR pulse energy (synchronized to the particular laser pulse that generated the SFG pulse), and the IR pulse energy in μJ , and their statistics. These data, along with system status messages are sent to the user interface via the inter-thread messaging architecture and displayed as graphs or text. If logging is enabled, the processed data is also sent to a logging thread which saves the data to disk during idle time.

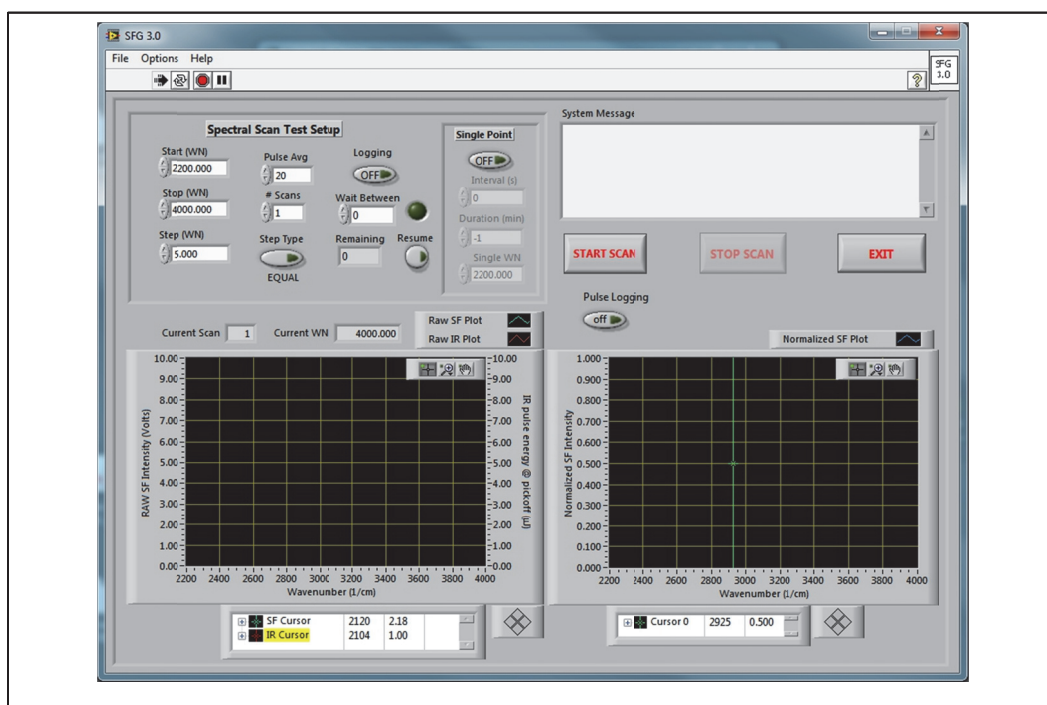


Figure 1.3 - SFG 3.0 User Interface. Scan parameters are set up in the upper left corner, system messages appear in the upper right corner. The raw SFG signal, and IR pulse energy (at the pickoff) are plotted in the lower left corner. The IR normalized SFG is plotted in the lower right corner. A typical scan steps from 2800 – 3600 cm^{-1} by 5 cm^{-1} , and each step acquires 200 SFG pulses. A single spectrum is acquired in about 45 minutes.

1.5.4 Single Crystal Ice Growth



Figure 1.4 – A “raw” ice boule after extraction from the glass crucible. The boule is about 25 mm dia. X 130 mm long.

Single crystal ice was grown in a Bridgeman-Stockbarger⁶⁵ apparatus (see Section 2). Temperature was controlled via a software based Proportional Integral Derivative (PID) control algorithm that resulted in a ± 2 milli-Kelvin stability. Crystal growth rate was held to 100 nm per second. The ice boules averaged 24.5 mm in diameter and 8.5 cm long. Growth yield exceeds 90% single crystal boules. The growth process is discussed in more detail in Sections 2 and 3. Samples were initially cut from the boule using a home built circular saw fitted with a home built 4-degrees of freedom fixture.

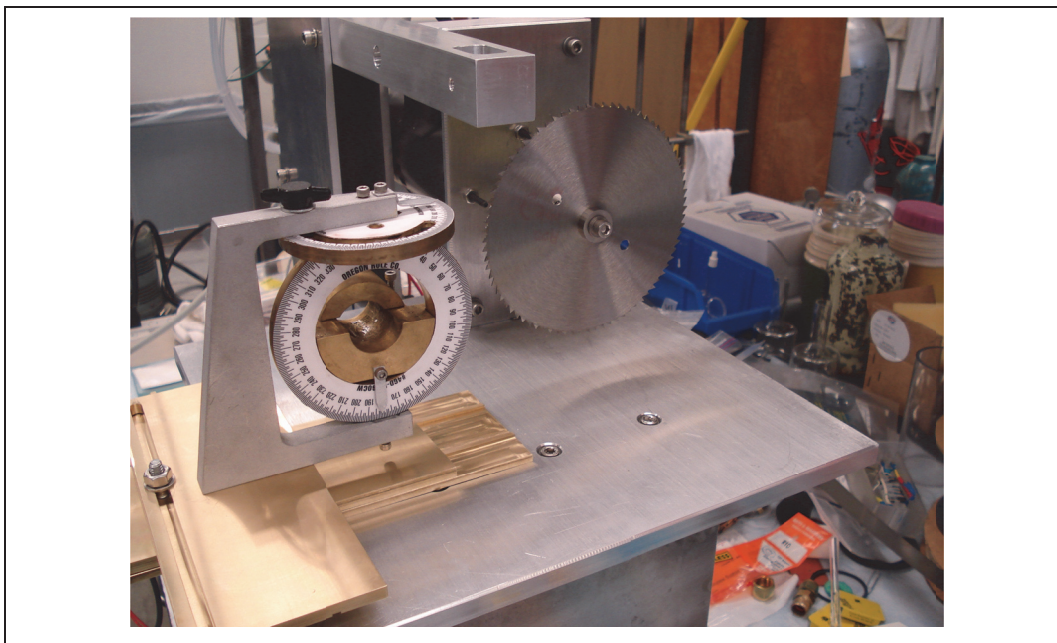


Figure 1.5 – Home built ice saw. This circular saw replaced a 3-wheel band saw. Changing to a clean-able circular saw proved critical to achieving low hydrocarbon contamination. The 4-degree of freedom ice boule fixture can be seen in the foreground. Pictured here on the workbench at room temperature, the saw and fixture normally reside in the -20 °C freezer.

1.5.5 Selection of crystal plane

A two-stage iterative process was used for *c*-axis orientation determination. First, a Rigsby^{66,67} stage was used to approximately determine the crystal *c*-axis and the boule sawed to expose the desired crystalline face. The rough-cut sample was microtomed producing a smooth face, and then etched⁶⁸⁻⁷¹ with Formvar (Ladd Research, Inc.) as follows. The sample was mounted on a microscope slide and a smooth surface produced using a microtome. After about 30 minutes annealing, the sample was swiped with a cotton-tipped swab saturated with 2% Formvar (in 1,1-dichloroethane) solution and placed in a microscope that was itself contained in a -20 °C freezer. The stage of the microscope was counter-heated and maintained at -5 °C. While the sample etched, time-lapse photomicrographs of the etch pit patterns were recorded (**Figure 1.9**). Etch times

for acceptable pit size was ca. 5 minutes. Fine crystal orientation was determined using the geometry of the etch pits and a CAD program (ProgeCAD). The boule orientation was adjusted on the saw and a new sample cut to expose the desired crystallographic plane.

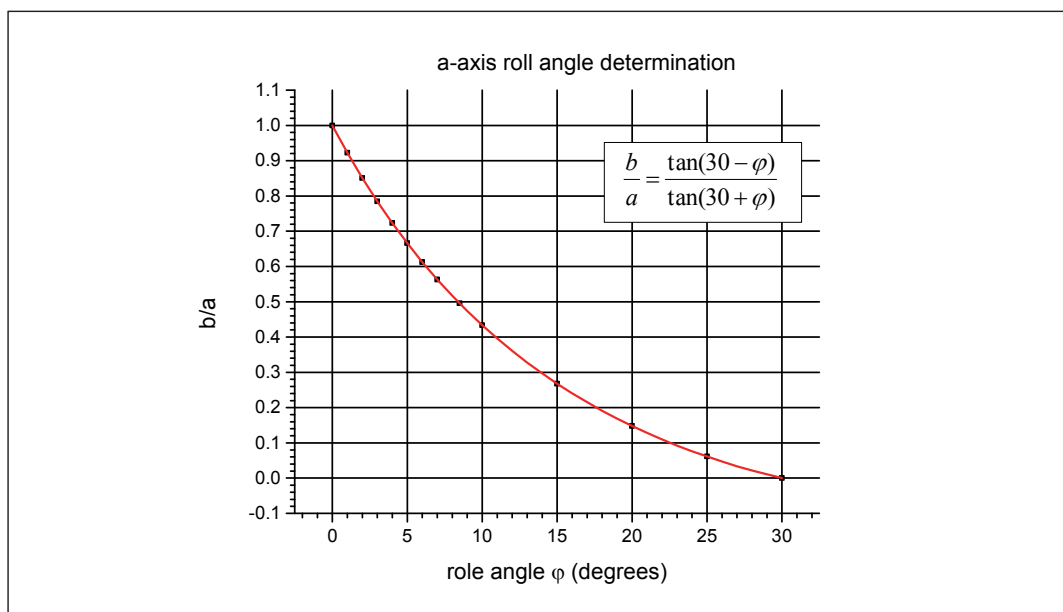


Figure 1.6 - a-axis roll determination for prism face samples. The ratio b/a is the longer to the shorter width of a prism face etch pit. See also **Figure 1.1** and **Figure 1.9**.

1.5.6 Sample Preparation

Once the optical axis of the ice was determined, a suitable prism or basal face sample was cut from the boule. Prepared ice samples averaged 8 mm thick \times 2.5 cm diameter with two 90 degrees apart reference flats for prism face samples, and approximately 8 mm thick \times 1.5 cm \times 2.25 cm rectangles for basal face samples. The surface was machined relatively smooth with a microtome (American Optical, Model 820) fitted with a disposable, diamond-coated blade (C. L. Sturkey, Inc.). The ice sample was subsequently mounted in an air-tight, all-glass cell with fused quartz windows and

the surface annealed at -20 °C for at least 48 hours producing an optically flat, low distortion surface.

1.5.7 Rigsby Stage

As indicated in section 1.5.5 a Rigsby^{66,67} stage (back-lighted crossed polarizers with a gimbaled sample stage between) is used to determine approximate c-axis orientation. This methodology makes use of the slight birefringence of single crystal ice.^{18,19} If the c-axis is oriented parallel to one of the two polarizer planes, the ice sample will appear to be dark (at an “extinction” point, or angle) when it is viewed between the crossed polarizers. If the c-axis is not parallel to one of these two planes, plane of polarization of the light passing through the ice sample will be rotated, and will then pass through the second polarizer to some degree. The result is that the ice sample will appear to be “illuminated”, or off an extinction point. If a sample has multiple domains, each domain will invariably have a unique c-axis orientation and the separate domains will be readily visible. **Figure 1.7** shows the Rigsby stage, **Figure 1.8** shows two examples of ice samples on the Rigsby stage. The sample on the left in the figure is single crystal and with its c-axis aligned parallel to one of the two crossed polarizer planes. It appears “dark”, with no additional illumination. On the right of the figure, another sample, grown without proper process controls, is polycrystalline and clearly shows how miss-aligned c-axis domains “light up” and easily become evident.

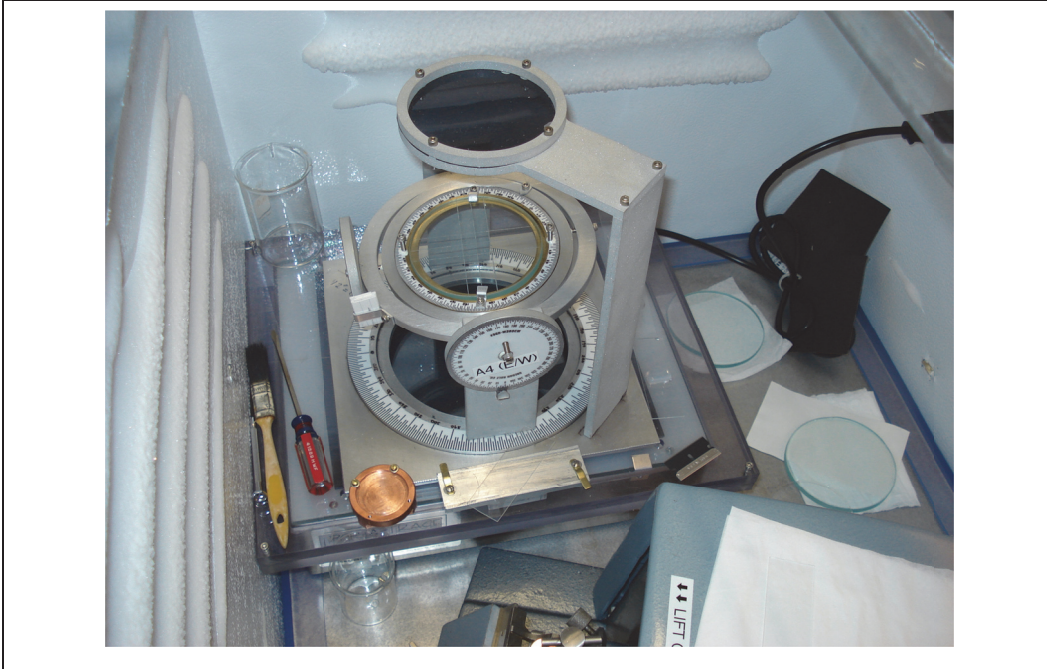


Figure 1.7 – Showing the Rigsby stage in a corner of the -20 °C freezer. A light-box at the base casts white light upward through a polarizer (large ring). The polarized light then passes through an ice sample (central, gimbaled ring). After passing through the sample, the (possibly rotated) plane polarized light passed through an analyzer (top ring) that is at right angles to the bottom-most polarizer. The geometry of the apparatus allows for four degrees of freedom.

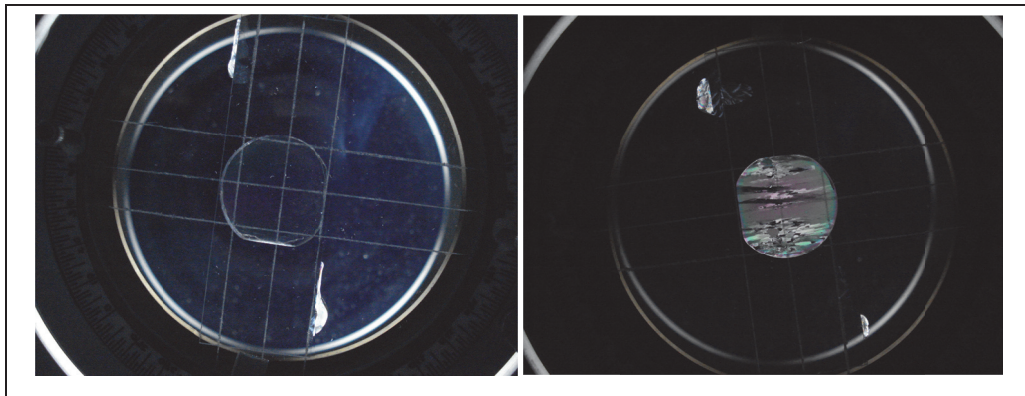


Figure 1.8 – Two prism face samples on the Rigsby stage. The perspective is looking down through the instrument, along the central vertical axis. LEFT: a single crystal sample with its c-axis oriented parallel to one of the polarizer axes. Note the c-axis is NOT along the reference flats, but at a small angle in this sample. RIGHT: a polycrystalline sample grown without proper process controls.

1.5.8 Formvar etching

After the optical axis is roughly determined, the boule is re-oriented on the saw so that the chosen face will be exposed. Because the c -axis is normally approximately perpendicular (± 20 degrees) to the boule axis, prism face samples tend to be circular (or elliptical) in outline. Conversely, basal face samples tend to be rectangular in outline. In order to verify more precisely the c -axis orientation, an initial rough cut sample is prepared by mounting it on a microscope slide and then the top surface is microtomed flat and smooth. **Figure 1.10** shows the microtome stored in the -20 °C freezer.

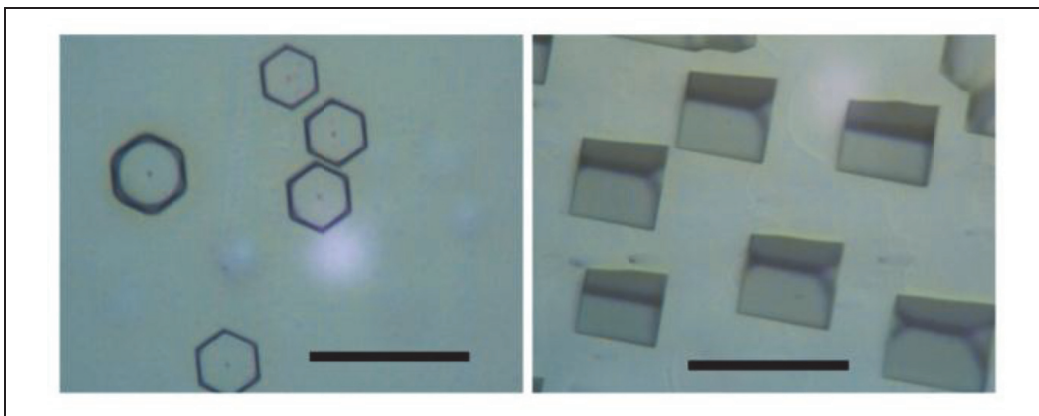


Figure 1.9 – Representative Formvar etchings of surfaces on the basal $\{0001\}$ plane (left) and the secondary prism $\{\bar{2}110\}$ plane (right). Based on pit shape, the basal plane is parallel to the surface to within 0.5° and the c -axis of the secondary prism surface (right) is parallel to the surface to within 3.0° . For the prism face (right), the a -axis “roll” angle off perpendicular is 3.6° . Scale bars are $100 \mu\text{m}$.

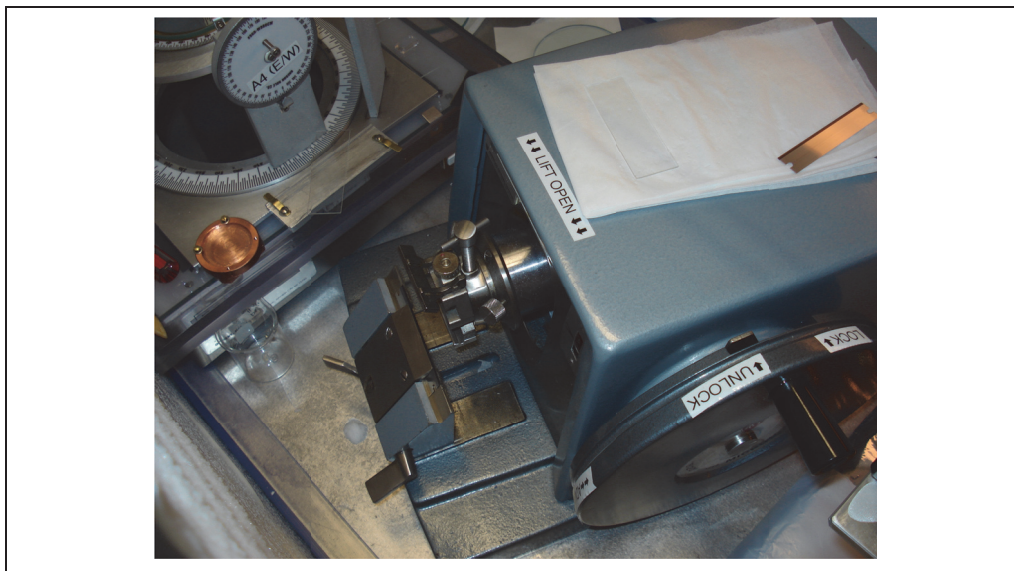


Figure 1.10 – Microtome in freezer. The crank handle (lower right) operates the head. A microscope slide and one of the disposable diamond coated blades can be seen on the folded white napkin on top of the machine. Disposable blades are a key part of reducing hydrocarbon contamination.

1.5.9 Sample mounting

Within the closed glass cell (**Figure 1.13**), the sample rested on a circular “carrier” consisting of a round copper ring, of rectangular cross section with a thin (0.002” thick) Copper membrane affixed to one side. The ice was laminated to the membrane via partial melting at the Cu/ice interface.

A freshly sawn sample of known orientation was prepared for mounting by first machining the back (or mounting) side using cleaned (with MeOH) Al₂O₃ sandpaper. The technique is to simply remove the saw striations, producing a smooth surface in preparation for fusing with the carrier membrane. After mounting in the carrier, the carrier is temporarily mounted on a carrier-to-microtome adaptor and the top face is shaved flat and smooth, using the microtome. The protocol is to shave a decreasing thickness series starting from 25 μm, stopping at 5 μm and in 10 μm steps. Several passes (ca. 10) of the microtome blade are performed at each thickness setting. This produces a

flat, smooth surface that will anneal to optical quality in ca. 2 – 3 days inside a closed cell.

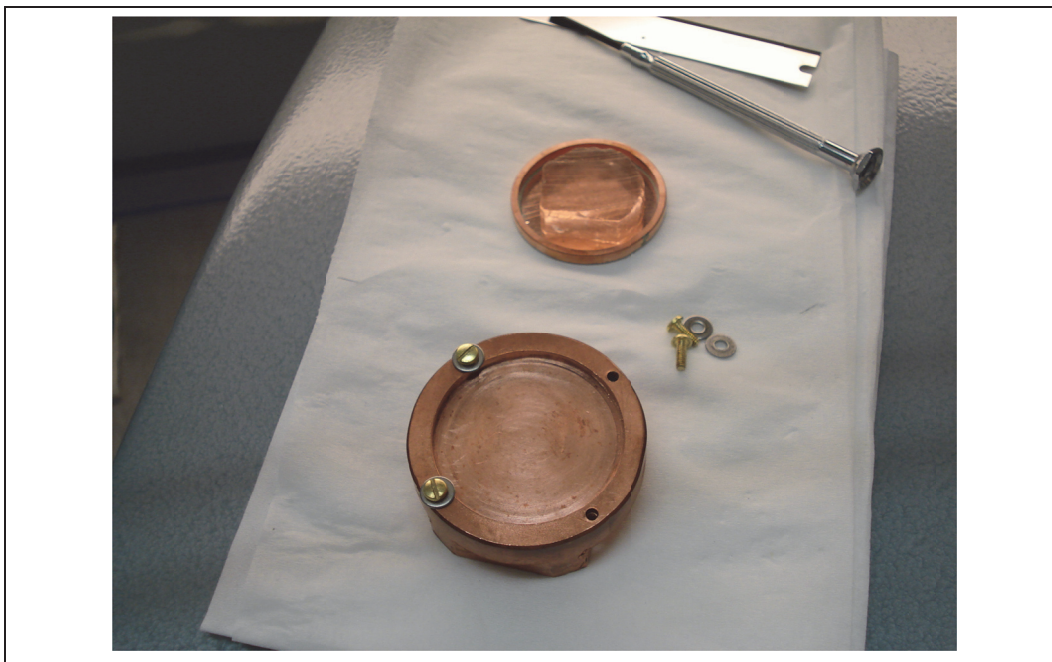


Figure 1.11 – Picture of a freshly sawn prism face, mounted in a carrier (top). The two reference flats, used to help with c -axis determination can be seen on the ice. The fixture used to grip the carrier and affix it to the microtome head is also shown (bottom). A portion of one of the disposable microtome blades can be seen (extreme top).

The carrier/ice assembly is clamped to the top of an oxygen-free-copper heat sink that extended out the bottom of the cell. The far end of the heat sink was immersed in liquid nitrogen, cooling the ice for measurement. This setup produced ice surface temperatures $-165\text{ }^{\circ}\text{C}$ to $-170\text{ }^{\circ}\text{C}$ as measured via a type T (Cu-CuNi) thermocouple embedded in the top surface. The glass cell had several ports to accommodate thermocouple wires, purge and dosing gases, etc. Without breaking the seal of the cell, the sample and heat sink could be rotated 90° to turn the sample from s (c -axis perpendicular to the input plane) to p (c -axis parallel to the input plane) orientation while at cryogenic temperatures.

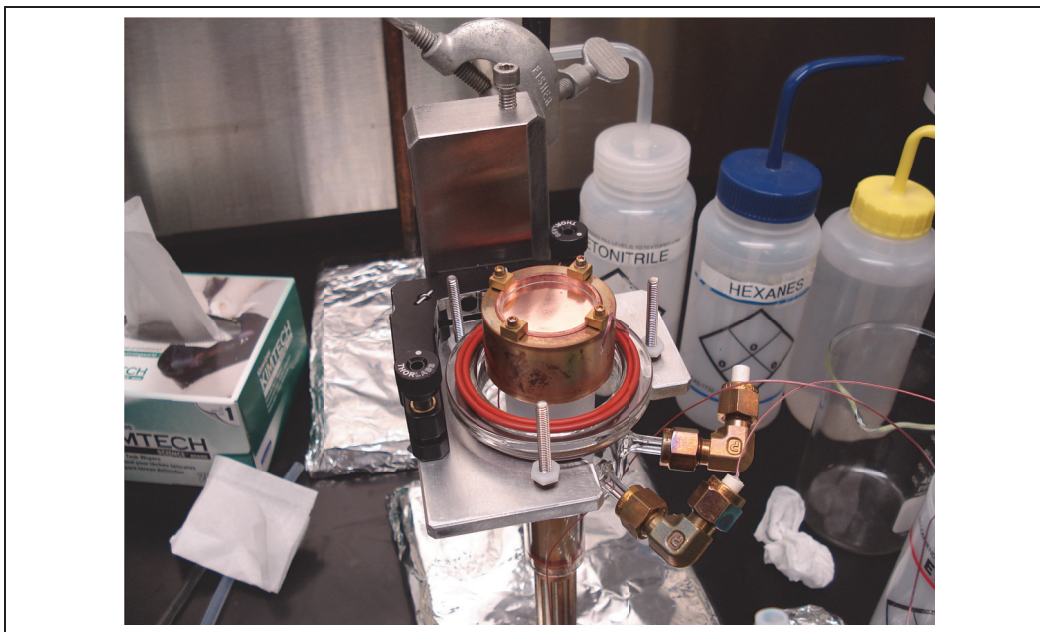


Figure 1.12 – An opened ice cell, at room temperature, on the workbench. The bottom half of the cell (glass) rests on a modified optical shelf kinematic stage and mounting plate. This provides fine pitch/roll control over the ice surface. A freshly made carrier is affixed to the top of the heat sink which extends out the bottom of the cell. The heat-sink flutes, critical for achieving low temperature operation (see Section 5.4), can be seen at the bottom. Two side ports on the glass bottom can be seen. One port is not in use, the other allows passage of a thermocouple to measure ice surface temperature.

Figure 1.13 (below) illustrates how the cell is aligned optically to the input lasers and output SF beams. The perspective is looking transversely (i.e.: along the $-Y$ axis) across the plane of incidence. The precision mirror mount (mentioned above) allows for pitch (rotation about the Y axis) and roll adjustment (rotation about the X axis). Azimuthal adjustment is accomplished by rotating the ice carrier, or the heat sink inside the cell. Z axis adjustment is accomplished via 1.5" post with a rack and pinion drive. X and Y adjustment is accomplished with a heavy duty translation stage.

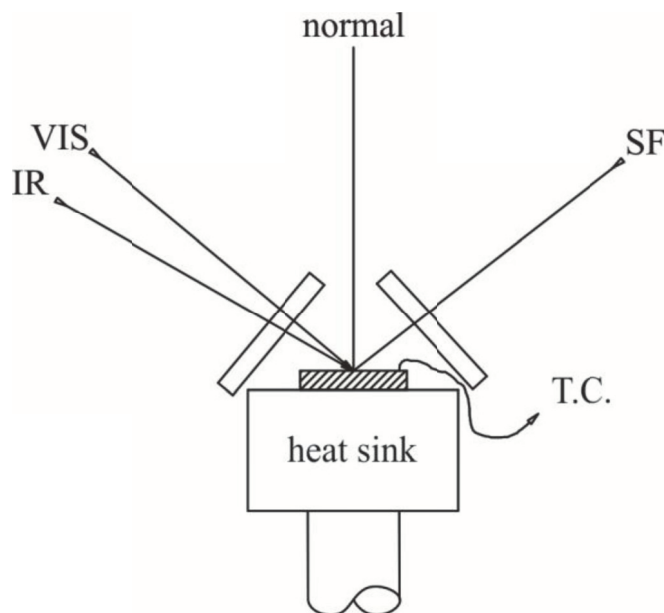


Figure 1.13 – Line drawing of ice sample within a closed glass cell. The body of the glass cell is omitted for clarity. The sample is mounted in a copper carrier, clamped to the top a copper heat sink that extends downward and is immersed in liquid nitrogen. The fused quartz windows are oriented roughly perpendicular to the beams. The ice sample (hatched field) is 8mm thick x 25mm dia. A type T thermocouple is imbedded in the surface of the ice about 1mm deep. The Vis and IR beams are at 50° and 60° angle of incidence, the SF beam is ca. 52°. Typical ice surface temperature is -165 °C.

1.5.10 Surface Hydrocarbon Determination

The protocol was validated for low hydrocarbon contamination by preparing test samples and measuring the *ssp* spectrum in the 2700 cm^{-1} to 3050 cm^{-1} region. Pulse energy levels could be increased slightly because ice is transparent in this band and the increased energy enhances detectability of any CH stretch mode. Detection limits were established by measuring an aqueous acetonitrile system in a closed cell with a 0.1x (mol fraction) acetonitrile concentration, sufficient to produce a 0.5x concentration at the surface⁷². Such a system produced easily detected CH stretching modes. Comparing this reference peak intensity to any potential peak detected on ice indicates the effective coverage. The lack of any detectable CH peaks in actual samples indicates an upper limit

of a very small fraction (e.g.: much less than 1%) of a monolayer for hydrocarbon contamination. See **Figure 1.14**.

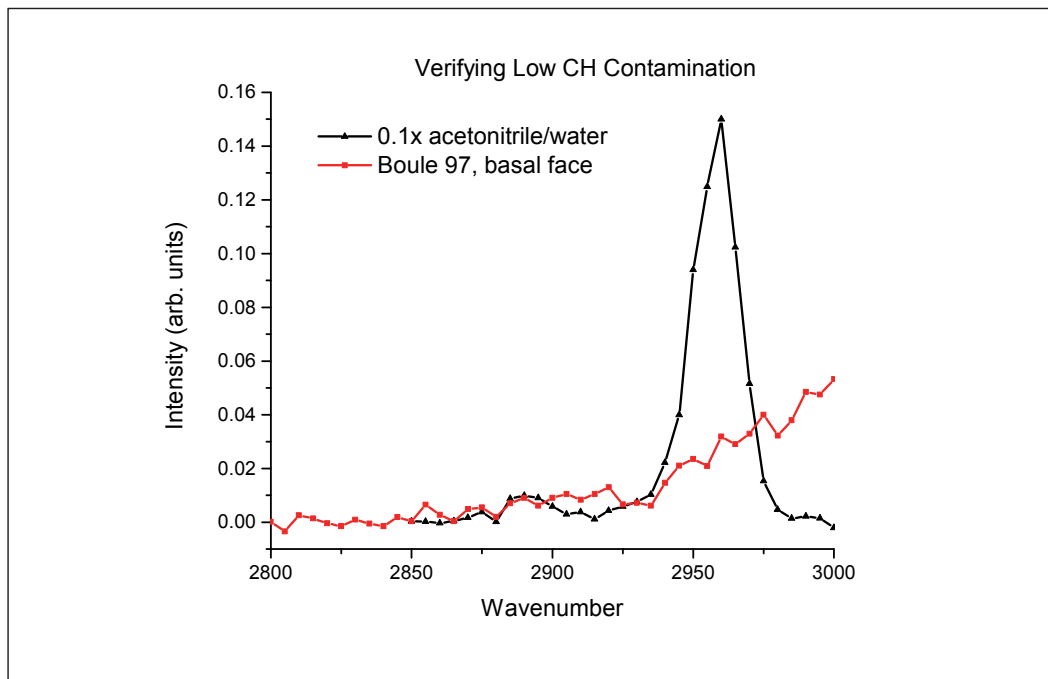


Figure 1.14 - Verifying low CH contamination. Both measurements are under similar experimental conditions (except temperature). This plot shows the 2800 – 3000 cm^{-1} band of a typical *ssp*, basal face ice spectrum (red, squares) as compared to a 0.5x acetonitrile concentration at the surface (black, triangles). The upward sweep for the ice data (at the blue end) is the skirt of the 3100 cm^{-1} peak which exceeds 1.56 in this data set.

1.6 SFG Results and Discussion

1.6.1 Spectra of basal face

Previous spectral studies of ice have focused on the basal $\{0001\}$ face.^{39-41,43,44} In particular, the sum frequency generation (SFG) spectra of the basal face in both *ssp* and *ppp* polarization have been published.^{39,41} The basal face has also been measured in the present work both as a general reference (**Figure 1.15**) and to provide an accurate

internal comparison with the prism face. The present measurements are in good agreement with Groenzin, *et al.*⁴¹

The *ssp* spectrum appears to be relatively simple with a strong feature at 3100 cm^{-1} and a shoulder at about 3200 cm^{-1} (**Figure 1.15**, left). A weak peak at about 3710 cm^{-1} , widely acknowledged to be due to the *d*-OH mode,⁷³ is also present, but falls out of band for this investigation. The *d*-OH, or “dangling OH” mode results from the uncoordinated OH bond present on the surface. Because it is not hydrogen bonded and extends into the vapor phase, the frequency of this mode is very nearly the same as the average between the symmetric and asymmetric vibrational modes of gaseous water,⁷⁴ 3706 cm^{-1} .

The *ppp* polarization combination shows a broader, more complex (i.e.: feature rich) spectrum (**Figure 1.15**, right). Specifically, there is a feature at about 3400 cm^{-1} (hereafter referred to as the “3400 cm^{-1} feature”), that has relatively low intensity, and stands apart from the rest of the spectrum. In contrast to the prism face, the 3400 cm^{-1} feature on the basal face is observed in the *ppp* spectrum, but is *not* present in the *ssp* spectrum, even when the intensity axis is expanded.

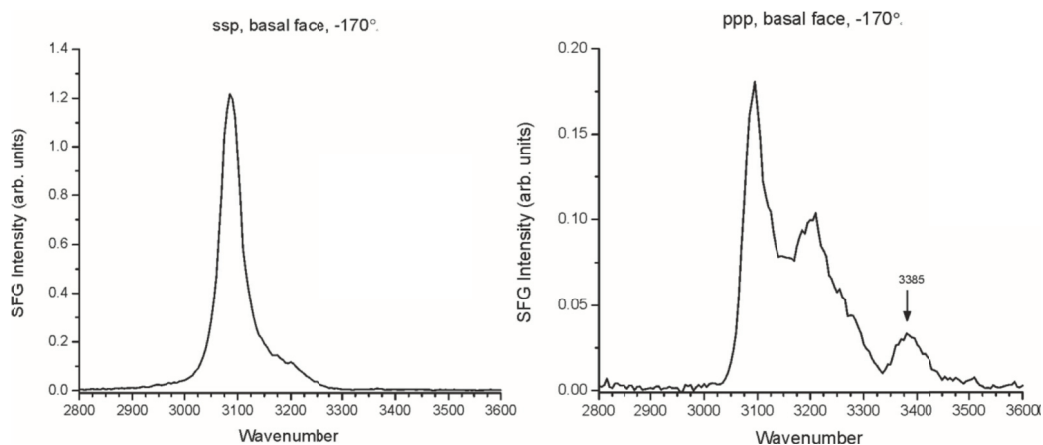


Figure 1.15 - The basal {0001} face of ice in *ssp* (left) and *ppp* (right) polarization. Note that the visible and IR intensities are the same for each spectrum, thus the surface produces a much weaker *ppp* than *ssp* spectrum. The

3400 cm^{-1} feature (actual 3385 cm^{-1}) is visible in the *ppp* spectrum, but not in the *ssp* spectrum. The amplitude of the *ssp* spectrum is ca. 6.8 times that of the *ppp* spectrum at 3100 cm^{-1} .

1.6.2 Spectra of secondary prism face

p-Oriented Secondary Prism Face

The secondary prism face presents richer features for the modes around 3400 cm^{-1} . Since the prism face is anisotropic, the crystal can be oriented either with the *c*-axis in the plane of incidence (*p*-oriented) or perpendicular to it (*s*-oriented). The 3400 cm^{-1} feature is sensitive to *s*- vs. *p*-orientation (**Figure 1.16** and **Figure 1.17**). Both orientations of the prism face produce spectra that are similar to that of the basal face, but with important differences. In *p*-orientation the 3400 cm^{-1} feature is visible in *ssp* polarization at about 3435 cm^{-1} . Further, this feature appears 50 cm^{-1} redder in *ppp* than it is in *ssp* (**Figure 1.16**).

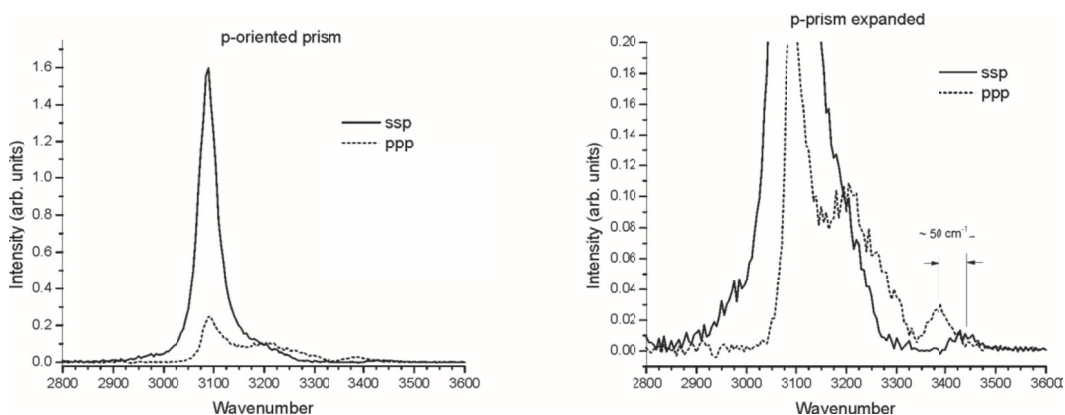


Figure 1.16 – A prism face, *p*-oriented, using *ssp* and *ppp* polarization combinations. Left: the two spectra showing relative amplitudes. Right: expanded ordinate-axis highlighting the 3435 cm^{-1} feature and the different modes observed with polarization.

s-Oriented Secondary Prism Face

When the crystal orientation is turned to *s*-orientation, the 3400 cm^{-1} feature is 30 cm^{-1} redder for *ssp* than it is for *ppp* (**Figure 1.17**): opposite to the observation in *p*-orientation. In addition to this reverse relationship, the frequencies of the peaks observed on the *s*-oriented interface are slightly redder than the *p*-oriented surface (Table 1.2).

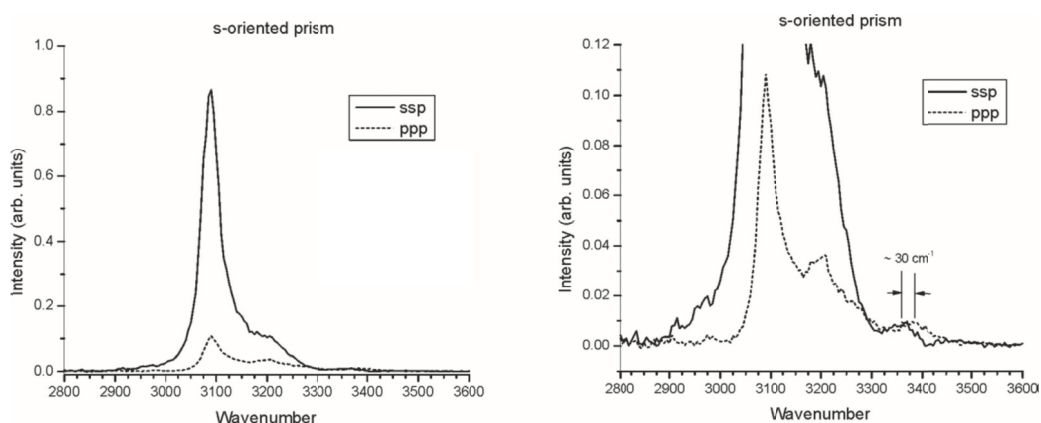


Figure 1.17 – A prism face, *s*-oriented, using *ssp* and *ppp* polarization combinations. Left: the two spectra showing relative amplitudes. Right: expanded ordinate-axis highlighting the reverse sense relationship with polarization and the redder frequency compared to the *p*-oriented surface.

Of some note is the relative intensity of the *s*-oriented spectrum with respect to the *p*-oriented spectrum. Close examination of the spectra shows that the *s*-oriented surface produces a signal that is about half the amplitude of the *p*-oriented surface. In all cases the energy densities at the surface were held constant, only crystal orientation or the polarization of the visible and SF beams changed.

Results from this 3400 cm^{-1} region are summarized in Table 1.2. Note that the frequency of the mode does not change due to changes in polarization or orientation. Rather, there are multiple modes of slightly different hydrogen bond strength and different orientation, each sensitive to a particular combination of polarization and crystal orientation.

Table 1.2 - Summary of results for the 3400 cm⁻¹ region			
Face	Orientation	Probe polarization	Mode (cm⁻¹)
Basal	NA	<i>ssp</i>	Not observed
	NA	<i>ppp</i>	3385
Prism	<i>p</i>	<i>ssp</i>	3435
	<i>p</i>	<i>ppp</i>	3385
	<i>s</i>	<i>ssp</i>	3385
	<i>s</i>	<i>ppp</i>	3415

1.6.3 Discussion and analysis

Identification of hydrogen-bonded resonances is critical for using vibrational spectroscopy to diagnose interactions and alteration of the hydrogen-bonded interactions with solutes. For water, the free-OH resonance was identified with the first SFG spectrum.⁷³ In contrast, the bilayer stitching bonds in ice have only recently been identified.⁴⁰⁻⁴² This work focuses on the weakest hydrogen-bond resonances on the ice surface near 3400 cm⁻¹.

In aqueous solutions, both the bulk and the surface respond to the presence of acids, bases, and salts.^{13,17,25,28,75-80} (Note the cited references are only a small sample of this large body of work.) Based on previous work, there is ample evidence that, in water, there is at least one bonding motif responsible for a prominent mode in the region of 3400 cm⁻¹. Whether more modes are involved remains a matter of some speculation and controversy. What is clear, however, is that these modes around 3400 cm⁻¹ represent weakly hydrogen-bonded species due to their position near the blue end of the hydrogen-bonded region. Identifying resonances at the surface of liquid water is very challenging due to a combination of short lifetimes and a plethora of accessible configurations. Single crystal ice, on the other hand, has high degree of order with a more limited and well defined number of bonding motifs. Thus, in addition to inherent interest in the ice

surface, ice is a model hydrogen-bonded surface facilitating assigning hydrogen-bonded resonances.

As the temperature of the ice falls below ca. -80°C , the SFG spectrum loses its broad-banded, featureless water-like character, becomes more feature rich and increases in intensity. Presumably this is due to the increased lifetime of the individual hydrogen bonds, thereby narrowing the line width of individual modes as well as limiting the number of accessible orientations.

Buch, *et. al.*²⁴ were probably the first to model the hydrogen-bonded region of ice using computational simulations of sum frequency generation. This facilitated a deeper understanding of the basal surface of ice but did not produce any firm spectral assignments. Groenzin, *et al.*^{40,41} measured the hydrogen-bonded region of the basal face using SFG and identified the 3100 cm^{-1} feature. Its apparent temperature sensitivity was found to be due to two closely spaced, overlapping modes that change relative intensity with temperature.

Based on observation of a significant quadrupole component, Groenzin *et. al.*⁴¹ assigned the 3100 cm^{-1} peak to the bilayer “stitching” bonds between layers on the basal face. Recently, Ishiyama and Morita, *et. al.*⁴² used MD simulation to explain both the high intensity and the quadrupole component of the reddest hydrogen-bonded feature, experimentally observed at 3100 cm^{-1} . In context of a relatively detailed understanding of the 3100 cm^{-1} feature on the basal face, this paper presents data and tentative assignments for modes near 3400 cm^{-1} that appear in SFG spectra of both the basal and secondary prism faces.

Discussion of the 3400 cm^{-1} Region

The liquid water SFG spectra contain at least two, broad features: one near 3200 cm^{-1} , the other near the 3400 cm^{-1} .¹⁴ The 3400 cm^{-1} region is of specific interest due to the

observation that its intensity increases upon addition of halide salts to water.^{14,81-83} Associating the altered intensity with changes in the water structure remains a challenge. Current efforts to construct this association include so-called phase sensitive (i.e.: complex) SFG measurements,^{84,85} which show that the hydrogen-bonded features are very broad, making it difficult to identify the resonances, much less associate those resonances with particular bonding motifs or interactions.

For ice, the 3400 cm⁻¹ feature is at the bluest end of the hydrogen-bonded region, so it is likely due to relatively weakly hydrogen-bonded species. Thus, the 3400 cm⁻¹ feature is generally thought to be associated with 3-coordinate water molecules in the top half bilayer. Three-coordinate molecules can either be double donors (also called *d*-O) or single donors (*d*-OH). The single donor OH is the companion to the free-OH and is expected to form a relatively strong hydrogen bond²⁴ and appear more toward the red end of the hydrogen-bonded region. Thus, all 3400 cm⁻¹ modes are tentatively assigned to double donors. The following presents an analysis with potential mode assignments based on this double-donor motif.

Basal Face

On the basal face of ice, all double donors are the same: all form donor bonds to four-coordinate molecules in the lower half of the top bilayer. Thus, as observed, the 3400 cm⁻¹ feature on the basal face is expected to be a single peak (**Figure 1.15**). These two donor bonds are necessarily out of the surface plane. Bond strain due to the dangling valence results in relatively weak hydrogen-bonds,⁸⁶ hence the OH stretch appears at the blue end of the hydrogen-bonded range. Because the dipole is out of the surface plane, there is a non-zero component of the dipole in the direction of the surface normal. Observation of, at best weak, intensity in *ssp* indicates that χ_{XXZ} is negligible. Since χ_{XXZ}

is negligible, it does not cancel χ_{zzz} (see Eq. (1.1.6)), the hyperpolarizability is largely longitudinal, and the mode is observed with only the *ppp* polarization combination.

Conclusion that the 3400 cm^{-1} peak is longitudinal is consistent with earlier reported polarization angle null (PAN) measurements.⁴¹ A largely longitudinal polarization is consistent with recent theoretical calculations⁸⁷ that, due to the dangling coordination (*d*-O), molecules in the top bilayer have a larger range of motion perpendicular to the surface. Hence changes in both the electric dipole and the polarizability are greatest perpendicular to the surface; thereby enhancing χ_{zzz} relative to χ_{xxz} . Thus, the 3400 cm^{-1} feature appears relatively intense on the basal face. There is only one possible choice of assignment in this case: the 3385 cm^{-1} peak observed only in *ppp* SFG on the basal face is assigned to the double donor, *d*-O motif. See **Figure 1.18**.

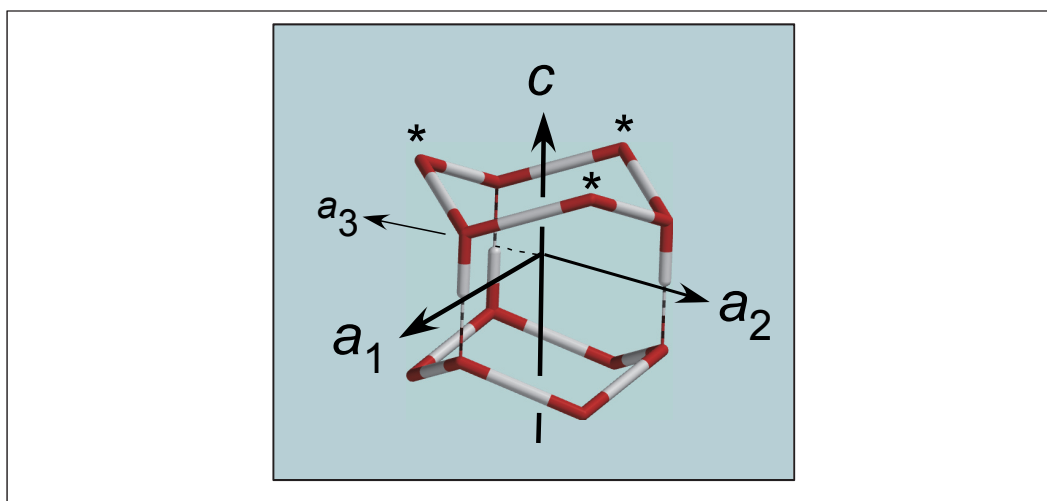


Figure 1.18 - View of the hexagonal ice structure of the basal face at the surface showing the “chair” water structure of the bilayers and bonding between two basal plane bilayers (stitching bonds). Top-half bilayer water molecules (starred) *may* have double donor OH bonds to the lower 4-coordinate molecules in the lower half of the top bilayer. Molecules with this bonding motif contribute to the 3400 cm^{-1} feature. Note that some, but *not all* of these (*) molecules are double donors. Some others but *not all* are single donors, giving rise to the *d*-OH bond.

Secondary Prism Face

Several different faces can be cut from the prism sides of the ice crystal. This work focuses on the $\{\bar{2}110\}$ or secondary prism plane (Figure 1.1). Because this face is also anisotropic, the crystal may be oriented with the c -axis parallel (p -oriented) or perpendicular (s -oriented) to the plane of incidence. On this face, the upper half of the top bilayer features dimers – two water molecules hydrogen bonded to each other. The remaining three coordinations consist of one dangling coordination and two bonds to the lower-half layer (**Figure 1.19**).

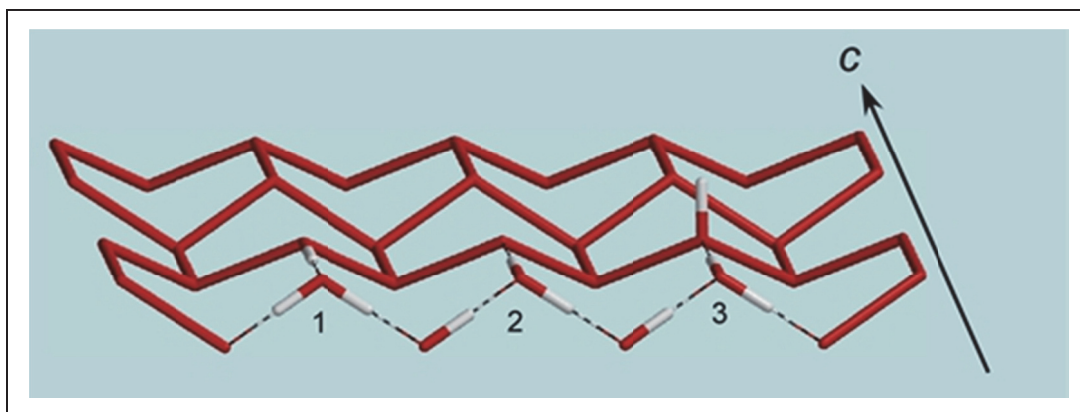


Figure 1.19 - Schematic of the secondary prism face explicitly showing the three bonding motifs of double-donor surface molecules: (1) double donor to four-coordinate water, (2) double donor with one coordination to a three-coordinate, double-donor molecule and one to a four-coordinate water molecule, (3) double donor with one coordination to a three-coordinate, single-donor molecule and one to a four-coordinate water molecule. Remaining structure is a schematic of the oxygen lattice. The c axis lies along the surface dimer bonds; the a -axis perpendicular to the surface.

Consider one molecule of the dimer, one with a d -O coordination; this molecule can be: (a) an acceptor from its dimer partner or (b) a donor to its dimer partner. If it is an acceptor (a), then both of its remaining coordinations must be donor bonds to four-coordinate molecules in the lower-half of the top bilayer. Because the donor OHs are

symmetrical, these two donors have a symmetric and an asymmetric combination. The asymmetric combination produces a dipole change parallel to the surface and is therefore SFG inactive for both *ppp* and *ssp*. This is because the IR beam is always polarized in the plane of incidence in our setup and cannot couple with the molecule. The symmetric mode is SFG active because the dipole does not lie in the surface plane and there is a component of the dipole along the *z*-axis and can couple with the *p* polarized IR beam. This is analogous to the motif on the basal face except that there is a mirror plane defined by the surface normal and the *c*-axis. Hence, the hydrogen-bonded resonance from those *d*-O, double-donor molecules is expected to be near 3385 cm^{-1} as it is on the basal face; though probably with different intensity.

The prism face provides an additional handle for definitive identification of this mode. In this case, since the *z*-axis component of the dipole change is the same without regard to crystal orientation, and the IR polarization is always *p*, the dipole itself does not help with mode identification. However, since the visible beam polarization may be changed, polarizability may be used to help with mode identification. The prism face can be oriented with the *c* axis in the plane of incidence, called *p* orientation, or with the *c* axis perpendicular to the plane, called *s* orientation. In *p* orientation, the symmetry axis of the double donor is in the input plane; in *s* orientation, the symmetry axis is perpendicular to the input plane. For individual water molecules, the polarizability of the symmetric stretch is largest along the symmetry axis, smaller in the molecular plane perpendicular to the symmetry axis, and much smaller perpendicular to the molecular plane.⁸⁸

In *p* orientation, the largest polarizability is in the input plane, the smaller one perpendicular to it. Accordingly, the 3385 cm^{-1} peak is observed when the stimulating electric field (i.e.: the visible beam) is in the input plane: i.e. in *ppp* polarization. It is weaker and not observed when the stimulating field is perpendicular to the input plane, i.e. *ssp* polarization.

Turning the crystal to *s* orientation rotates the largest polarizability perpendicular to the input plane. Hence the 3385cm^{-1} peak is observed when the visible beam polarization is perpendicular to the input plane, i.e. in *ssp* polarization. In analogy to the basal face bonding motif, the 3385 cm^{-1} resonance observed on the *p*-oriented, secondary prism face is assigned to these double donor water molecules on the surface.

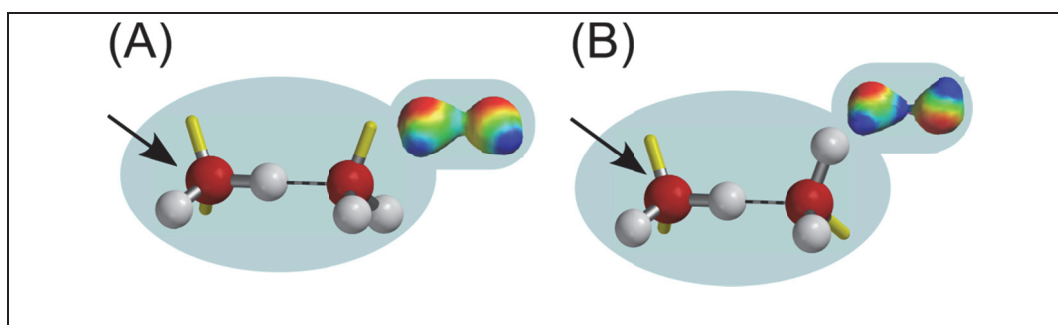


Figure 1.20 - Two configurations for the secondary prism face dimer: (A) the single-donor hydrogen bonds to a double-donor dimer partner (B) the single-donor hydrogen bonds to a single-donor, *d*-OH partner. Both the vibrational frequency and the polarizability of the single donor are altered by its dimer partner. Arrow indicates subject molecule. Upper right: electrostatic potential map.

In the second case (b), the subject molecule again has a *d*-O unsatisfied coordination but is a donor to its dimer partner (**Figure 1.20**). The molecule therefore has only one bond to donate to the next layer. The bond to the dimer partner, being parallel to the surface, is SFG silent. The bond down to the lower half of the top bilayer is SFG active. The crystal orientation and polarization dependence of this bonding motif suggests a spectral assignment as follows.

The dimer partner can have either a *d*-O (**Figure 1.20A**) or a *d*-OH (**Figure 1.20B**). These two configurations of the nearest neighbor, dimer partner likely influence the OH stretching frequency of the subject molecule. Further, the polarizability of the OH stretch is expected to be different in configurations (A) vs. (B) of **Figure 1.20**.

The spectra show two remaining un-assigned resonances: 3415 cm^{-1} and the 3435 cm^{-1} . Both modes have larger polarizability perpendicular to the c axis than along the c axis: the 3415 cm^{-1} mode has significant intensity only when the c -axis is perpendicular to the plane of incidence (i.e.: s -oriented ice) and the visible polarization is in the plane of incidence (i.e.: p -polarized). The 3435 cm^{-1} mode only has significant intensity when the c -axis is in the plane of incidence (i.e.: p -oriented ice) and the probing polarization (i.e.: the visible beam) is perpendicular to the c axis (i.e.: s -polarized). The 3415 cm^{-1} mode appears to be a longitudinal mode: its ZZZ hyperpolarizability is larger than its XXZ hyperpolarizability. In contrast, the 3435 cm^{-1} mode appears to be a transverse mode: its XXZ hyperpolarizability is larger than its ZZZ hyperpolarizability.

Correlating the experimental hyperpolarizability orientation conclusions in the immediately preceding paragraphs with the dimer picture illustrated in **Figure 1.20** suggests the following assignment. With two vertically oriented dangling lone pairs, the polarizability of the dimer illustrated in **Figure 1.20(A)** is strongly longitudinal and the oscillating dipole is nearly along the subject molecule next-layer donating OH bond, essentially perpendicular to the c axis. Hence, the 3415 cm^{-1} mode is tentatively assigned to motif (A). The oscillating dipole of motif (B) is similarly nearly perpendicular to the c axis, but its polarizability is more tangential. The 3435 cm^{-1} mode is thus tentatively assigned to motif (B). Testing these tentative assignments awaits further experimental and/or theoretical work.

It should be mentioned that there are other potential assignments for the 3415 and 3435 cm^{-1} modes. For example, on the other side of the subject molecule shown in **Figure 1.20**, the donor coordination up from the bottom-half layer can also be SFG active. Since such donor molecules are four coordinate, the hydrogen bonds formed are expected to be strong and thus strongly red shifted, i.e. more in the 3200 cm^{-1} region. Similarly, the d -OH partner shown in **Figure 1.20B** has a similar bonding orientation as

that of the subject molecule, thus has similar SFG activity. However, the hydrogen bond between the companion OH and the lower-half of the top bilayer (i.e.: the 4-coordinate molecules) tends to be of low strain. This lower strain produces a stronger hydrogen bond and therefore greater red shift. There is some speculation²⁴ that this bonding motif may be associated with the 3200 cm^{-1} feature common to all the *ppp* spectra. For these reasons, the assignments indicated in the preceding paragraph are favored. Future theoretical and experimental work will likely test these assignments.

1.7 Conclusion

The unique attributes (i.e.: polarization, orientation, and relative phase interference) of SFG plus the highly periodic nature and low thermal energy of cryogenic, single-crystal ice and dissimilarities between the isotropic basal face and the anisotropic prism face has been used to obtain several mode assignments on the surface of the basal and secondary prism faces. The peak appearing at 3385 cm^{-1} is assigned to three-coordinate, double-donor (with *d*-O) water molecules in the top-half of the upper most bilayer on the basal face and the similar double donor to four-coordinate water on the prism face. Observed peaks appearing at 3415 cm^{-1} or 3435 cm^{-1} are assigned to those three coordinate (with *d*-O) molecules on the surface that have only single donors to the 4-coordinate molecules in the bottom half of the top bilayer. Sorting the 3415 and 3435 cm^{-1} modes is more tentative. Current experimental evidence favors assigning the 3415 cm^{-1} mode to dimer pairs, both of which have dangling lone pairs. The 3435 cm^{-1} mode is assigned to pairs consisting of a dangling lone pair and a dangling OH. Further testing and resolution of these last assignments await further experimentation and/or theoretical study.

1.8 Future work

Future experimentation could include a similar set of experiments e.g.: SFG , focused on the primary prism face. The primary prism face has at least one additional bonding motif that includes long zigzagged H-bonded chains in the top half of the top bilayer. This is in contrast to the hexagonal chairs of the basal face, or the dimers of the secondary prism face.

Future experimentation could include carefully controlled surface dosing experiments. Several attempts were made in this research to dose the surface with probe molecules like methanol, sulfur dioxide, and ethanethiol. However, none of the dosing experiments produced any result other than a general suppression of the spectrum. The exact reason for this result is undetermined. One would expect to observe characteristic changes in the SFG spectrum caused by the presence of a probe molecule on the surface.

In terms of crystal growth, more boules should be grown and their crystal orientation fully determined. Although nearly 100 boules have been grown, the process changed over time and has only recently stabilized. The statistical sample size for fully oriented boules (that is, those whose crystalline orientation was fully characterized using optical and etching methods) using the new growth protocol is still rather small (about a dozen). The tendency of the a-axis to be oriented along the boule axis is not very well understood. More statistical data in this area could shed some light on the problem.

Recently single crystal boules have been sent to Prof. Ian Baker of the Thayer School of Engineering, Dartmouth College, Hanover, New Hampshire. Recent communication with Prof. Baker indicates the samples demonstrated anomalous mechanical properties and that he would like more samples to follow up on this line of research. This shows another area for future research. That is, simply growing and supplying high quality single crystal ice to other ice researchers. Ready availability of large, verified single crystal boules could be a boon to ice research.

2 Ice Growth Apparatus

2.1 Introduction

Of critical importance in this research is the ability to manufacture, reproducibly, the material of interest: low defect density, single crystal ice. Some considerable effort has been put into finding a practical solution to this important problem. Various methods of growing single crystal ice have been described by a number of researchers^{18,19,49,89,90} and further described by Groenzin and Li.^{91,92} With the exception of Groenzin and Li, very little is made of the difficulty in accomplishing the task. However, it is clear from the level of effort devoted to growing single crystal ice in this laboratory, across (now) three graduate student careers and more than a decade here at the Shultz laboratory, that a high yield process is no small accomplishment.

One key accomplishment by Groenzin and Li^{91,92} is the development, design and construction of the basic modified Bridgeman-Stockbarger apparatus adapted for the production of ice. The modified design incorporates two concentric, cylindrical baths of ethylene glycol and a “shelf” with a hole in it, centrally located within in the inner bath, dividing it into two communicating volumes. A stepper motor and controller provide the mechanical drive to lower a glass crucible into the apparatus.

The inner bath is static and it does not circulate. The shelf divides the inner bath into two regions: upper and lower. In the upper region, a coiled heating element, near the periphery of the inner bath, maintains a temperature above freezing. The lower region has no such heater and is allowed to come into thermal equilibrium with the outer bath via conduction through the wall of the inner bath. The outer bath circulates through a chiller that maintains a constant temperature below freezing. Due to the effects of the counter

heater, and the below freezing outer bath, a temperature gradient is set up within the inner bath. When the counter heater power and outer bath set point temperature are set correctly, a 0 °C “surface” can be confined to the hole in the shelf. In this way, the volume above the hole, the ethylene glycol is above freezing. In the volume below the hole, the temperature is below freezing.

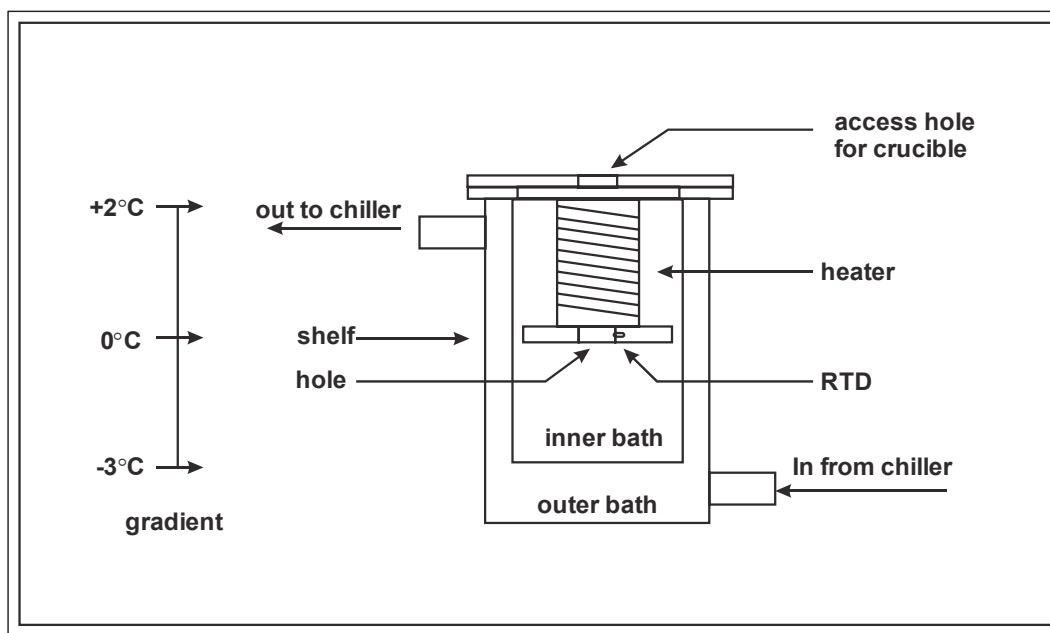


Figure 2.1 – Diagram of inner structure of modified Bridgeman-Stockbarger apparatus. The outer bath sets the low temperature at -3 °C; the counter heater sets the 0 °C surface. The 0 °C surface is “pinned” within the hole of the shelf by software control. The counter heater establishes a temperature gradient as shown on the left.

In order to grow ice, a cylindrical glass crucible that contains highly purified water, is slowly lowered into the inner bath without rotation, and through the hole in the shelf by the stepper motor drive system. The water freezes as the crucible is lowered through the zero degree “surface” confined to the hole. Crystallization is nucleated by the introduction of a polycrystalline “seed” induced to form in a small capillary at the very bottom of the crucible by super cooling to the point of freezing with a methanol/dry ice (ca. -78 °C) bath. After growth is complete, we call the resulting plug of ice in the

crucible a “boule”, in a manner similar to the growth of large single crystal semiconductor boules.

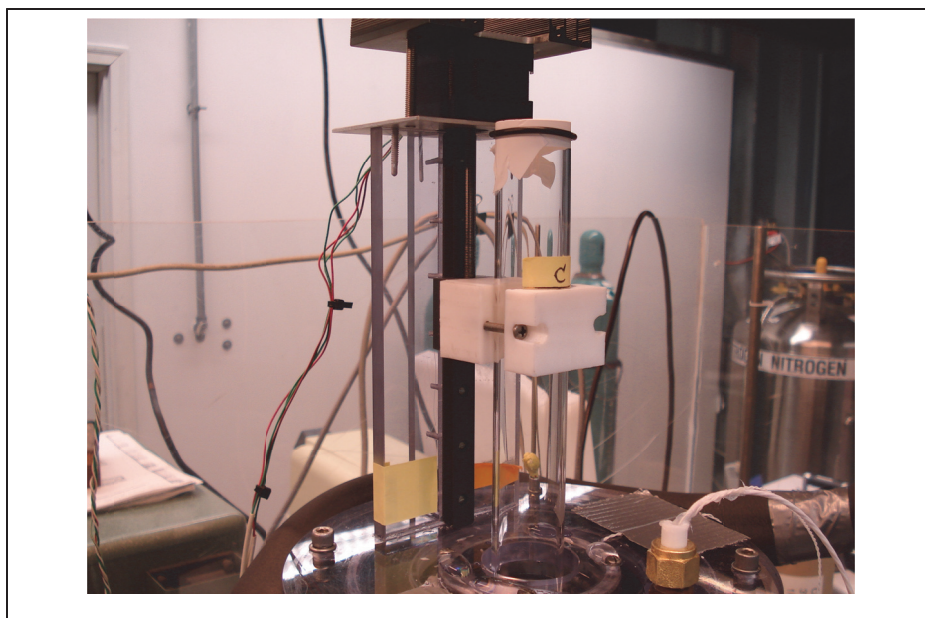


Figure 2.2 – Picture of top of ice growth apparatus showing drive system and an ice crucible. The ice growth process is mid-way in this photograph.

As one would expect, the velocity of the crucible through the freezing zone, outer bath temperature, counter heater power, and temperature stability of the room, outer bath, and inner bath all play critical roles in single crystal, single domain production yield. The work of Li and Groenzin produced a set of conditions that gave a rough yield of 10% for single crystal, single domain boules. However, such a low yield coupled with the extended length of time it takes to grow a boule, has a strong negative influence on “experimental throughput”, greatly hindering the rate of research. One of the major contributions of this research is the improvement of the basic Modified Bridgeman-Stockbarger machine itself, establishment of appropriate operating conditions, and establishment of stable production protocols that yield single crystal, single domain, ice boules with a yield in the range above 90%. **Figure 2.3** below shows the block diagram of the final system.

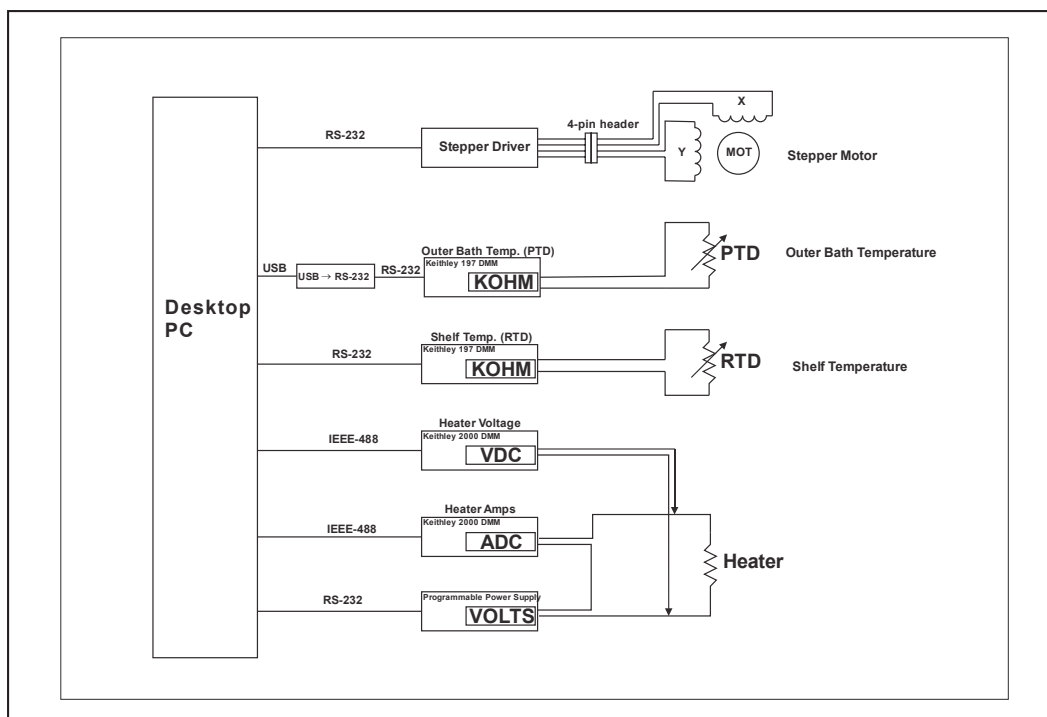


Figure 2.3 – Block diagram of ice growth apparatus. A desktop PC communicates with several DMMs using RS-232 and IEEE-488 protocols. Two DMMs read the resistance of an RTD or a PTD and convert that to temperature. Two DMMs read the voltage and current applied to the heating element inside the apparatus. The shelf temperature (RTD) is used as feedback to the PID control algorithm. Control is established by commanding the B&K Precision Model 9130 programmable power supply to a new voltage.

2.1.1 Modified Bridgeman-Stockbarger

The Bridgeman-Stockbarger technique^{65,93} of making single crystals involves moving a crucible filled with the liquid phase through a zone of cooling that incorporates a temperature gradient. In moving through the temperature gradient from above the melting point to below, a crystal of high purity and quality is grown. In comparison to Stockbargers' original geometry, the current design geometry is essentially identical. But the current geometry is essentially upside down with respect to designs typically used in growing single crystal semiconductors. In the semiconductor design, the melt is in the lower part of the crucible and the solid phase is in the top. The temperature gradient is

from hot at the bottom of the apparatus, to cool at the top of the apparatus. The crystal is grown by slowly pulling the crucible out of the melt.

In the Stockbargers' and the present design, the solid phase is in the bottom of the crucible, and the liquid phase is at the top. The crucible motion is downward from the warm part of the apparatus, through the freezing zone, into the cold part of the apparatus.

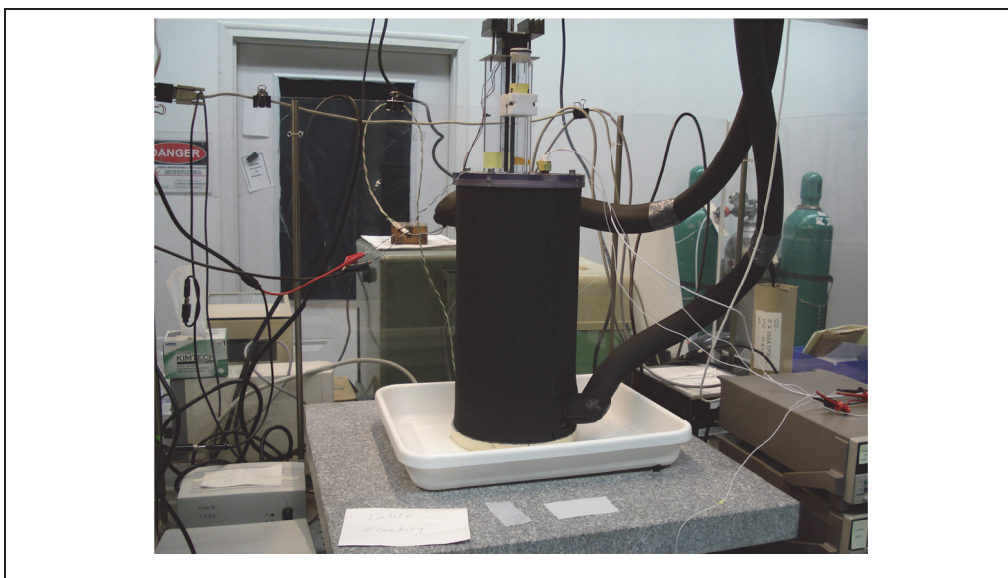


Figure 2.4 – The fully insulated Modified Bridgeman-Stockbarger apparatus sits on a 3-foot square piece of granite, floating on three air pillars for vibration isolation. Supply and return hoses (5/8" ID) circulate 70%wt ethylene/glycol at -3 °C and at nearly 23 L/min. The drive system and a mounted crucible can be seen at the top.

2.1.2 Internal construction

In order to establish a temperature gradient, a counter heater is used in the upper half of the central, static ethylene glycol bath. This heater is a very simple helical winding of 24AWG NiCr wire, insulated with PTFE “spaghetti” tubing. Electrical connections are provided by crimped butt-splices that interface stranded, insulated copper wire. A crimped connection is necessary because NiCr wire (a kind of stainless steel)

cannot be “wet” by solder, so directly soldered connection between NiCr and Cu is not possible.

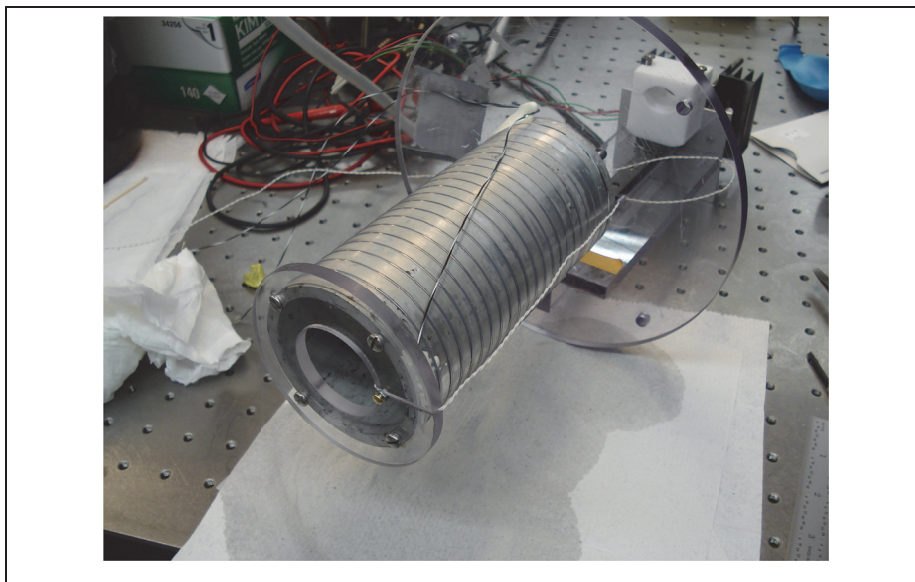


Figure 2.5 – Showing the internal structure of the apparatus. The counter heater is the aluminum tube wrapped with NiCr wire. The shelf with its hole and RTD can be seen at lower left. The crucible clamp and drive system can be seen in upper right.

At the bottom of the counter heater, a circular “shelf” made from $\frac{1}{4}$ ” thick polycarbonate is attached. The shelf has a concentric hole that allows the crucible to pass through with a small gap (ca. $\frac{1}{4}$ ”) around its periphery. The finite thickness of the shelf is important. The thickness allows for a small volume within which to “pin” the $0\text{ }^{\circ}\text{C}$ surface via computer control. If the shelf were too thin, no degree of computer control could pin the $0\text{ }^{\circ}\text{C}$ surface within the hole and the $0\text{ }^{\circ}\text{C}$ surface would “flutter” above and below the hole with even the smallest external temperature variation.

The shelf does not fit tightly within the inner bath. Instead, there is a small gap (ca. $\frac{1}{4}$ ”) between the edge of the shelf and the wall of the inner bath. This gap, coupled with the small gap between the hole and crucible allows for a continuous temperature gradient within the hole that is not too steep. If the temperature gradient within the hole is

too steep, crystal flaws will develop and secondary domains may also become established. The exact magnitude of the gradient has never been measured. Instead, practical experience with crystal growth under varying gradients (which can be inferred qualitatively) indicates a small gradient promotes higher quality boules.

2.1.3 Chiller

A chiller sets the outer bath temperature. It is a Thermo/NESLAB RTE 740 Digital Plus model with heating and cooling capabilities. It uses an internal Proportional/Integral/Differential (PID) temperature control mechanism. The PID control constants were optimized from the factory defaults to account for the length of the hoses connecting the chiller to the outer bath. Because of the finite coolant flow rate, it is possible to cause the temperature control to become unstable and temperature oscillations can result. This is the case for the factory default PID control constants and they were adjusted heuristically to provide maximum stability and minimum thermal response time.

The hoses that connect the chiller to the outer bath are also important for optimum system performance. Originally, these hoses were 1/4" OD x 3/16" ID plastic tubing. Also, they were laid up adjacent to each other, within a common insulating sleeve. This configuration essentially formed a crude counter-flow heat exchanger structure, in direct opposition to the function of the chiller. The small hose diameter unnecessarily restricted flow rates to ca. 4 L/min.

During a re-build operation of the whole ice growing apparatus, the connecting hoses were changed to 5/8" ID hoses and all the pipe fittings were replaced with those appropriate for 5/8" ID hoses. This significantly reduced pump back pressure and allowed the flow rate to increase to nearly 23 L/min, the maximum flow rate the chiller

can provide. Additionally, the routing and insulation of the hoses was changed so that each hose was individually insulated, reducing the heat exchange effect.



Figure 2.6 – Picture of the Thermo/NESLAB RTE 740 chiller. The coolant supply and return hoses (black, insulated) can be seen at the rear. The chiller specific electronic control (a PID) is seen mounted on top of the machine. The chiller set-point is $-3.3\text{ }^{\circ}\text{C}$.

Also during the rebuild, the outer insulation of the outer bath was enhanced. Originally only two layers of expanded LDPE at about $\frac{1}{2}$ " thick, the insulation was changed to two layers of $\frac{5}{8}$ " thick expanded butyl rubber for a total thickness of $1\frac{1}{4}$ ". With the above mentioned changes in the system, the apparatus was able to produce outer bath temperature stability of ca. $\pm 0.02\text{ }^{\circ}\text{C}$ even though the room temperature varied by as much as $\pm 5\text{ }^{\circ}\text{C}$.

2.2 Modified Bridgeman-Stockbarger computer control

As mentioned in Section 1, a key innovation in the high yield production of single crystal ice is the imposition of computer temperature control. The methodology is a feedback technique commonly known as a Proportional Integral Derivative, or PID algorithm. PID's have become quite common in many types of industrial process control. This includes temperature control, flow control, position, velocity, etc.. A PID can be implemented in hardware, in a strictly analog sense or even a digital sense. A PID can also be implemented in software, especially if the process can be controlled with periodic sampling. And, this is the case for the ice growing process, which is controlled by measuring the temperature at the shelf, and making an appropriate adjustment in the programmable power supply for the heater once every ten seconds.

2.2.1 PID

A block diagram of the PID algorithm is given below:

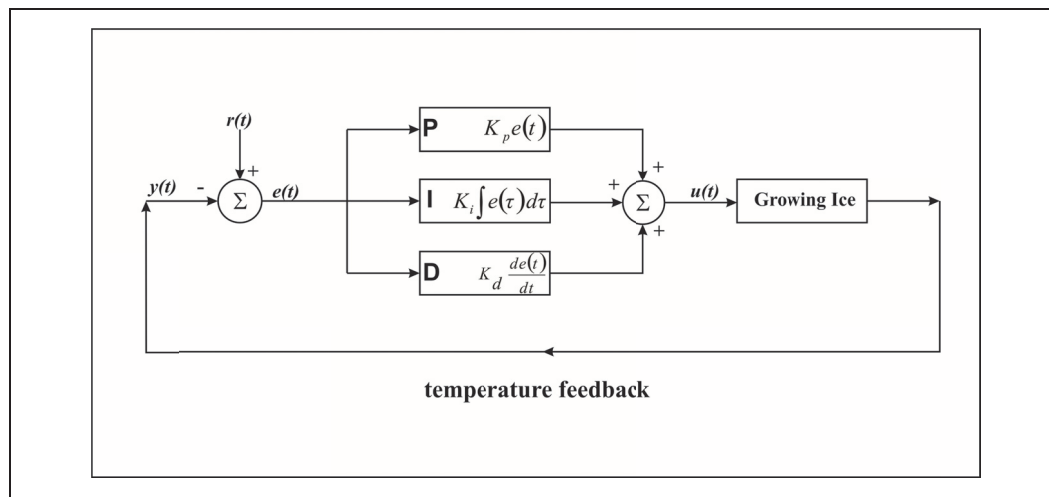


Figure 2.7 – The PID algorithm as applied to the ice growing process. The measured temperature $y(t)$ (“output” of the process) is fed back negatively to the input. It is summed against the setpoint temperature $r(t)$ to generate the error signal, $e(t)$. The error signal, $e(t)$, is processed in three ways: 1) the “present” 2) the “history” or the “past”, and 3) the “future” or “predictive”. These three generated signals are then summed and used to derive a new control signal, $u(t)$, to drive the process (shelf temperature) closer to the setpoint.

In the process of growing the ice, that which can be controlled is the temperature at the shelf, and specifically the temperature in the hole of the shelf. The more stably this temperature can be held, the better. The measured temperature is designated $y(t)$ (“output” of the process) is a periodically sampled value and is fed back negatively to the input. At the input, $y(t)$ is summed against the desired setpoint temperature $r(t)$ to generate the error signal, $e(t)$. That is, $e(t) = r(t) - y(t)$. The error signal, $e(t)$, is processed in three ways: 1) the “present” 2) the “history” or the “past”, and 3) the “future” or “predictive”. It is these three ways of processing the error signal that gives the PID algorithm its power. The error “in the present” is scaled by K_p . The historical error or the history of the system is represented by the scaling (K_i) and integration of the errors from the past, up until “the present”. Finally, a “prediction” of the error in “the future” is made by scaling (K_d) and differentiating the error in the present. These three generated signals are then summed and used to derive a new control signal, $u(t)$, to drive the process (shelf temperature) closer to the setpoint. The actual signal $u(t)$ is a text command sent to the programmable power supply that powers the counter heater within the ice growing apparatus. If the shelf temperature is above the setpoint, the power supply is commanded to generate a lower voltage (reduce the power) and the inner bath cools slightly. If the shelf temperature is below the setpoint, the power supply is commanded to generate a higher voltage (increase the power) and the inner bath warms slightly. In this way, the temperature at the shelf, in the hole of the shelf, is controlled to the +/- milli-Kelvin levels.

The PID control coefficients were determined by a heuristic process. A series of step changes in setpoint were commanded and the response of the system was noted. First the proportional constant (K_p) was adjusted, then the integral constant (K_i) was adjusted, and finally the differential constant (K_d) was adjusted. The goal for acceptable performance was when the shelf temperature showed only a single overshoot past the

setpoint and a minimum settling time to within +/- 0.002 Kelvin. **Table 2.1** lists the final PID control coefficients.

K_p	70.00
K_i	10.00
K_d	3.00

2.2.2 Software (general)

The software used to control the temperature of the ice growing apparatus is called “Ice Machine Temperature Controller” and is currently at version 1.3.2.1. The software is written in LabVIEW 8.51 and incorporates the mentioned PID algorithm, a user interface, a logging function capable of automatically indexing file names, and the ability to interface with two DMMs (to sense the power supply voltage and current) via a IEEE-488 bus, a DMM that measures the resistance of the RTD (located in the shelf) via an RS-232 protocol, a DMM that measures the resistance of the PTD (located in the outer bath) also via an RS-232 protocol, and finally the B&K Precision Model 9130 programmable power supply via a third RS-232 interface.

The software converts the non-linear, negative temperature coefficient RTD resistance to temperature in °C and the linear, positive temperature coefficient PTD resistance to temperature in °C for use in various places in the program. **Table 2.2** and Table 2.2 list the calibration coefficients for the RTD and PTD respectively.

Y0	1902.791490
----	-------------

A	30700.879280
t0	18.748120

To obtain these coefficients, the resistance vs. temperature of the device was measured and then curve fit using the following exponential function:

$$T_{RTD} (\text{°C}) = Y0 + Ae^{(-R/t0)} \quad (2.1)$$

Where: R is the measured resistance in ohms.

In the case of the Omega Model PMA PTD, the resistance vs. temperature function is linear but the resistance vs. temperature curve still has three coefficients:

R0	100.167500
α	0.003925
<i>offset</i>	0.167500

And the temperature is found by the following equation:

$$T_{PTD} = \frac{(R - offset)}{(R0 * \alpha)} - \frac{1}{\alpha} + offset \quad (2.2)$$

Where: R is the measured resistance in ohms and *offset* compensates for lead resistance.

The user interface of the Temperature Control Software is shown in **Figure 2.8**. The interface allows for changing of the most frequently adjusted parameters. However, the software also uses a Windows “INI” file to store all the calibration coefficients and other options. The INI file is located in the same directory as the program.

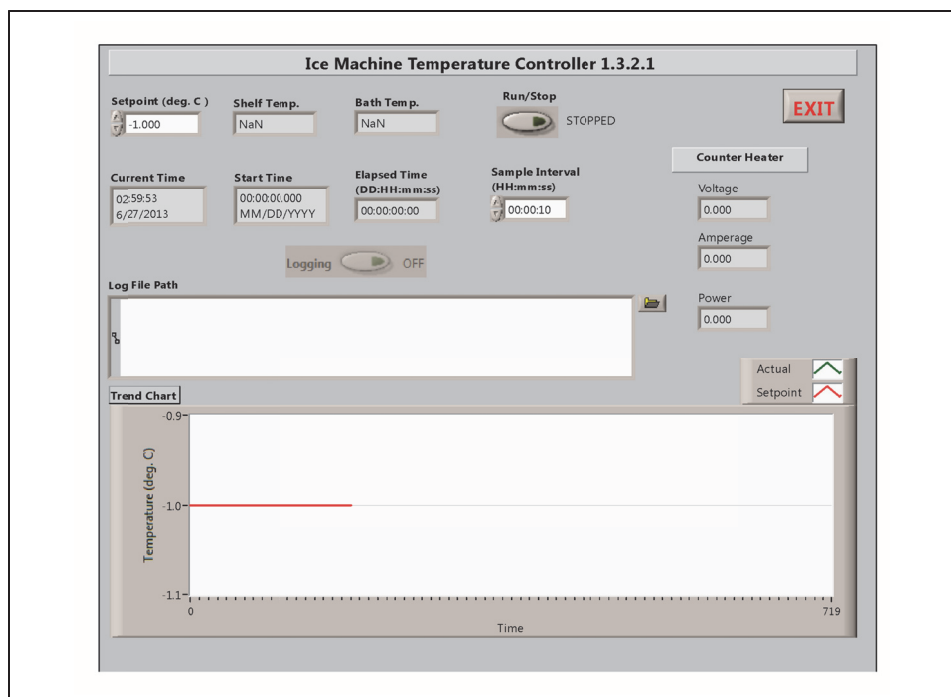


Figure 2.8 – Ice Machine Temperature Controller Software user interface. The desired shelf temperature setpoint (normally -1 °C) is adjusted in the upper left. If a log file name is provided, the “Logging” button is enabled and the logging function may be started. The “Run/Stop” button enables the temperature control function. The counter heater Voltage/Amperage/Power is indicated along the right hand side. A strip chart indicates the recent history of shelf temperature as compared to setpoint along the bottom of the interface.

2.3 Degassing

It has been found through experience that if the water in the crucible is degassed, defect density and the tendency to form multiple domains within the boule are greatly reduced. The original degassing operation took place under ultrasonic agitation. However, standing acoustic waves have been observed to trap small gas bubbles within the water column. Because of this, the ultrasonic agitation step has since been discontinued.

The present degassing operation utilizes a mechanical vacuum pump and vacuum line to reduce the pressure within the crucible to about 20 torr. The crucible is immersed

in an ice/water bath contained in a high quality Dewar, thereby lowering and pre-chilling the crucible in preparation to ice growth.

Originally, the degassing operation lasted only 35 min.⁹² However, it has been found that the diffusion constant of many gases, including CO₂, N₂, and O₂ is only on the order of $1.5 \times 10^{-5} \text{ m}^2/\text{s}$ ^{94,95} and, when coupled with relatively low dissolved mole fraction of about 2×10^{-5} for each gas at 0 °C,⁹⁶ a half hour of degassing at 20 Torr most likely does not significantly reduce the dissolved gas content, especially since the water column is nearly 18 cm deep. With this in mind, the degassing operation was extended by a factor of four to two full hours.



Figure 2.9 – Water degassing vacuum line. The ice crucible is connected to the hose with the adaptor at upper right. The bottom of the crucible extends into the glass Dewar (lower right) filled with ice/water. A water trap can be seen at lower center held within the stainless steel Dewar filled with LN₂. The mechanical vacuum pump is seen at bottom left of center.

3 Ice Growth Habits

3.1 Introduction

Once the ice production process stabilized, and the number of single crystal, single domain boules increased, a number of trends were observed. First and foremost was that the c-axis was typically oriented nearly perpendicular to the boule axis (i.e.: the c-axis was parallel to the ice/water growth interface). This seemed to be in close concordance with the analysis of Ketcham and Hobbs⁴⁹ who give experimental evidence and an explanation based on surface tension (surface energies) of two adjacent crystallites where one “edges out” the other. Of some importance, their experimental setup is very close to our growth setup: using a moving crucible, capillary, polycrystalline seed and even crucible velocity. They conclude, through this selection process, ice grown from the melt will have a preferred orientation where the c-axis is parallel to the solid/liquid interface. Their analysis focusses on the grain boundary at the solid/liquid interface and the relative c-axis orientation of the two grains with respect to the boundary and the solid/liquid interface.

Essentially, Ketcham and Hobbs explain that if the c-axis of a grain is more closely oriented to perpendicular to the grain boundary than an adjacent grain, and is more steeply oriented to the solid/liquid interface, it will be “edged out” by the adjacent grain. Thus, the grains that survive this selection process are those whose c-axis is parallel to the growth surface. If two grains have an equal degree of parallelism to the solid/liquid interface, then the grain with its c-axis closer to perpendicular to the grain boundary will be “edged out”. Eventually, only a single domain remains, or possibly two domains with c-axes nearly parallel, but perpendicular to the domain wall. This last condition has been observed in our apparatus on several occasions. See **Figure 3.1**.

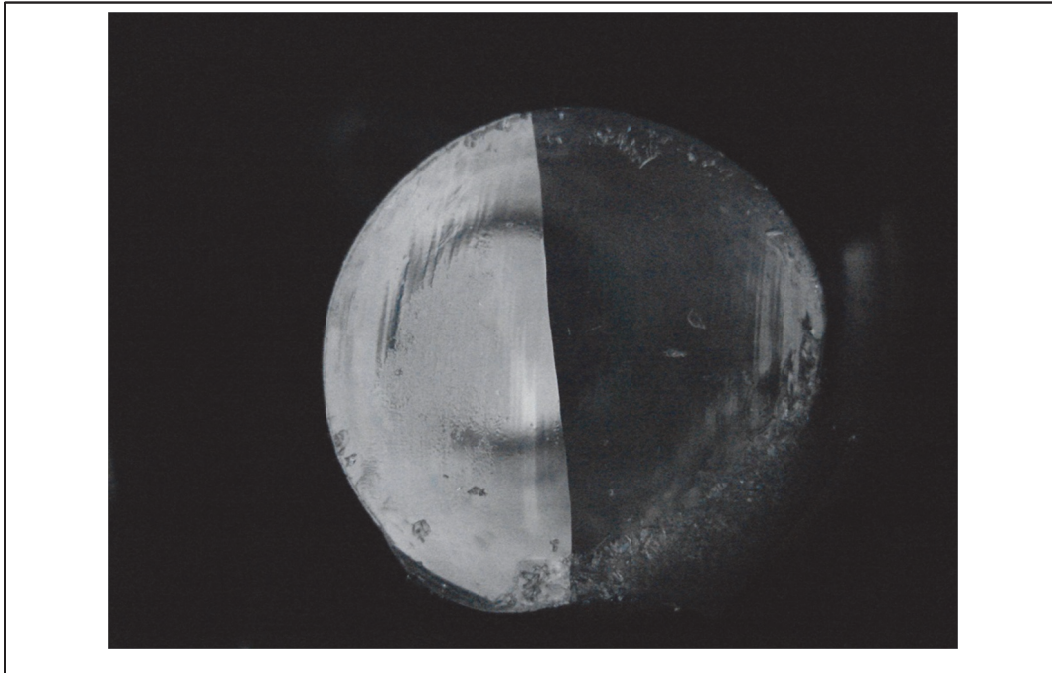


Figure 3.1 - A double domain boule viewed end-on in the Rigsby stage. This was a case where both c-axes are nearly perpendicular to the domain wall, and also perpendicular to the boule axis. The long optical path (a full 10 cm) makes this test quite sensitive to c-axis orientation. Only a few degrees difference in orientation between the two domains can show one ‘extinct’ and the other to be ‘bright’.

Another observed growth habit is that the a-axis (see **Figure 1.1**) showed a marked tendency to orient perpendicular to the ice/water growth interface within the crucible. This tendency became apparent when we began high precision orientation using Formvar etching. With this tendency, a “bologna” sliced sample from the boule naturally displays a secondary prism face. This tendency is not as strong as the c-axis orientation (100%), but it is still quite strong. More than 70 or 80% of the single crystal boules presented a secondary prism face to within 10° . At the present, this growth habit cannot be explained directly by the experimental results of Ketcham and Hobbs^{48,49}, or Libbrecht⁹⁷ who indicate the differences in solid/liquid surface energies, or growth rates in the case of Libbrecht, between the faces are small.

By examining the different faces it is easy to see that the secondary prism face should have a slight entropic edge over either the basal or primary prism faces. Both the basal and primary prism faces must assemble larger groups of molecules to complete their faces. The basal face must assemble a hexagon chair, and the primary prism face must assemble long zigzag chains of molecules, that is, they both incur an entropic penalty during assembly. The secondary prism face needs to only assemble non-contiguous dimers and so the surface might have a slightly higher energy. With this description, and in the context of Ketcham and Hobbs⁴⁹ description, the secondary prism face could have a very slight edge in terms of selection bias over the primary prism face. And, this is our experimental experience: Significantly more than half of all boules present a secondary prism face at the solid/liquid growth interface.

A third characteristic was that the optimal growth velocity seemed to be very much slower than growth velocities often quoted in the literature⁹⁸⁻¹⁰⁰ from numerical studies and experimentation. Rozmanov⁹⁸ did MD simulations looking at growth rates as a function of temperature and size of model (number of molecules in the simulation) for growth from the melt. He indicates a maximum rate at about 7 cm/s under super cooled conditions. Pruppacher⁹⁹ also indicates experimental rates on the order of 10 cm/s, but again, under super cooled conditions and specifically for dendritic growth. Furukawa¹⁰¹ gives dimensionless growth rates, but again for dendritic growth. More recently, Shibkov¹⁰⁰ has measured dendritic growth rates as a function of supercooling with a similar maximum rate on the order of 10 cm/s.

Without surprise, the growth rate (velocity) is dependent on the degree of super cooling. But in our apparatus, the degree of super cooling is not expected to be greater than one tenth or at most a few tenths of a degree C. Thus, the growth rate in our apparatus is expected to be quite low due to this low level of super cooling. In fact, when our apparatus is set to grow ice at rates greater than about 100 nm/sec, macroscopic

defects develop in the boule, and even secondary domains form that obviously haven't been nucleated in the capillary.

3.2 Seed crystal

The seed crystal is formed in situ in the small bulb at the end of the capillary at the bottom of the crucible. See **Figure 5.1**. A pre-charged (with water) crucible is pre-chilled by placing it in the ice growth apparatus for one hour. This insures the crucible and its contents have the same temperature profile as the apparatus. After one hour, the crucible is removed and the bulb at the end of the capillary is partly immersed in a methanol/dry ice bath (-78 °C). This cools the bulb and a small clump of poly-crystalline ice is formed at the bottom of the capillary. Thus, there is no single seed. Instead, the growth process starts from many seeds, and with many different orientations. This type of seed is identical to that used in the work of Ketcham and Hobbs.⁴⁹

3.3 Temperature stability

Temperature stability in the region of the growth interface plays an important role in the growth of high quality crystals. Given the temperature gradient within the hole of the shelf, any change of temperature locally will shift the 0 °C surface up or down to some degree. If the 0 °C surface moves upward, the growth interface will experience increased super cooling and the growth rate will increase. If the surface moves downward, the super cooling will decrease and growth will slow. If the rate increases too much, randomly oriented micro-crystallites can form and become occluded when the temperature returns to normal. This leads to a kind of flaw that has been dubbed "feathering" because of the feather-like lenticular structures that can be observed inside the boule when it is viewed in the Rigsby stage.

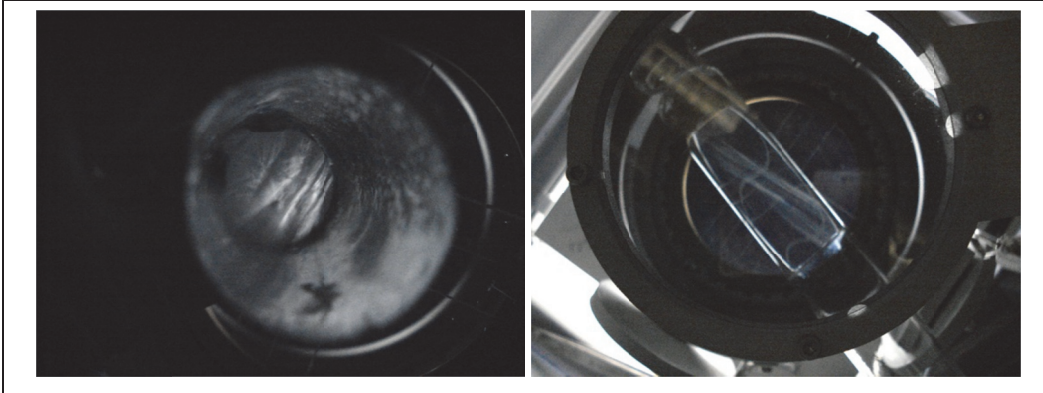


Figure 3.2 - Feathering in a boule. Left: Viewing a boule end-on in the Rigsby stage, the “feathers” form multiple, parallel planes. Right: Viewing (a different boule) side-on. This type of flaw was completely eliminated after positive temperature control was implemented.

3.4 Temperature gradient

Too steep a temperature gradient from the top of the apparatus, to the bottom, gives greater propensity to nucleate a new domain. And, the steeper gradient makes the instrument more sensitive to variations in temperature both inside the apparatus at the shelf, and to the external room temperature. As the gradient increases, the degree of super cooling increases for a given crucible velocity and growth rate increases. This leads, again, to increased propensity to nucleate secondary domains.

After much experimentation, it was determined that a total gradient of from -3 °C at the bottom of the inner bath to $+3$ °C at the top of the bath, with the 0 °C surface in the center worked well. To get this gradient, the chiller is set to give an outer bath temperature of -3 °C, and then the heater is adjusted to get the shelf temperature at 0 °C. If the top of the bath was then too warm, the outer bath ethylene glycol/water concentration was changed to increase its water content. Increasing the water content of the outer bath increases its thermal conductivity and heat capacity. If the top of the inner

bath is too cool, the water content of the outer bath is reduced (by exchanging some of it with pure ethylene glycol).

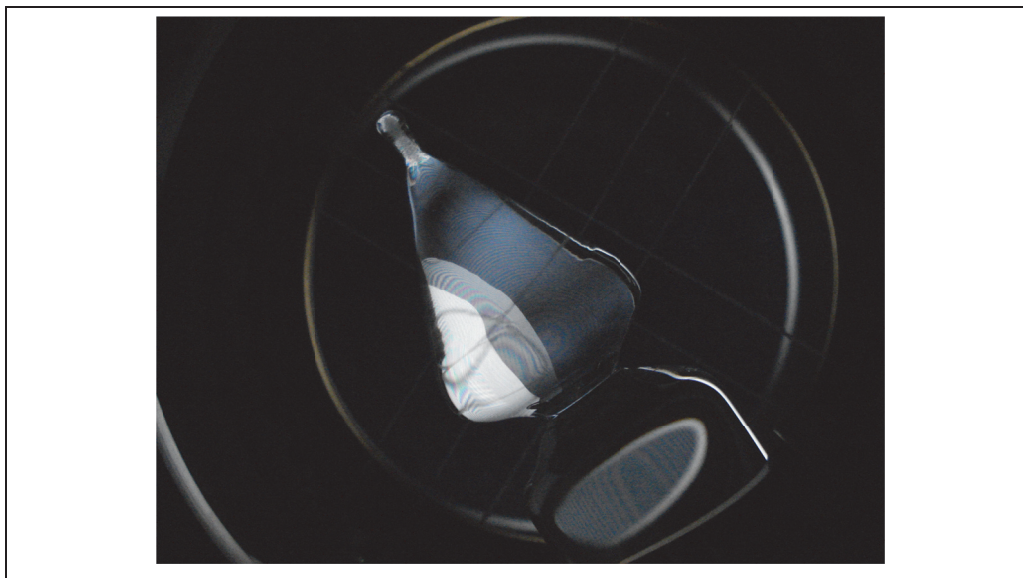


Figure 3.3 - A secondary domain. This is a picture of the bottom end of the crucible, freshly out of the growth apparatus, viewed in the Rigsby stage. The polycrystalline seed can be seen in the capillary (upper left). The primary domain of the boule is oriented so that it appears ‘extinct’ (dark). The secondary domain has an odd orientation and so appears ‘bright’. It is clear that the secondary domain has nucleated along the inside surface of the glass crucible and is not connected with the primary seed in the capillary.

One of the great revelations in this work was that the entire boule could be examined in the Rigsby stage. And, in fact the boule need not be extracted from the crucible. When this was realized, regular examination of the domain structure near the capillary, and in the ‘bulb’ below the neck greatly enhanced the understanding of how the capillary, bulb and neck were functioning to select out unwanted domains. Examination of the full boule to determine if it was single domain, and even get a rough idea of the c-axis orientation was a big help when selecting a boule for experimentation. Prior to full boule examination, a boule candidate had to be cut up and each slice examined in the Rigsby stage. This was a very time consuming process and sometimes was all for naught when the boule was determined to be unsuitable for experimentation.

4 Summary

The prism face of single crystal ice I_h has been studied using sum frequency vibrational spectroscopy focusing on identification of resonances in the hydrogen-bonded region. The polarization capabilities of sum frequency generation (SFG) were used in conjunction with the crystal orientation to characterize three vibrational modes visible at 3400 cm^{-1} . These modes are assigned to three-coordinated water molecules in the top-half bilayer having different bonding and orientation motifs for either the basal face, or the secondary prism face.

Such mode identification is only possible with the production and use of single crystal ice of very low defect density and of size appropriate for examination using the SFG technique. Production of single crystal ice is often trivialized in the literature. But in reality, large single crystals are very difficult to produce. Design and construction of an apparatus and protocol that can produce large single crystals of ice truly advances the state of the art. An apparatus utilizing the Bridgeman-Stockbarger method of single crystal growth was designed, constructed and optimized for the growth of ice. This design features a software implemented (LabVIEW) Proportional-Integral-Differential (PID) feedback temperature control algorithm. The temperature at the growth interface was controlled to within $\pm 0.002\text{K}$ even though room temperature variation was ca. $\pm 2\text{K}$.

Since the measurement must occur at cryogenic temperature (ca. 130K), the design and construction of a cell that can enclose and isolate the ice sample from ambient conditions is also of critical importance. An air tight, all glass design was chosen that incorporates two fused IR quartz windows to allow for visible and mid-IR transmittance, an oxygen free copper heat sink and a unique ice mounting scheme.

The thermal design of the heat sink and ice mount are critical for reaching cryogenic temperatures and ensuring the ice sample remains attached to the heat sink as the temperature is lowered. A “carrier” consisting of a thin copper membrane soldered to a copper ring functioning as a frame provides mitigation of thermally induced stress on the ice and at the same time, provides excellent thermal conductivity with the heat sink.

The heat sink was optimized to incorporate “flutes” which provide sharp edges, or asperities that disrupt a nitrogen vapor barrier forming at the copper/LN₂ interface due to the Leidenfrost effect. Without the flutes, the vapor barrier is persistent enough to keep the ice at the top of the heat sink from achieving low temperatures. With the flutes, the vapor barrier is defeated because the asperities cool to below the “Leidenfrost threshold” and initiate a broader scale cooling of the heat sink to below the threshold. The result is that the sample can be cooled to much lower temperatures.

Growth of a large number of boules (ca. 100) has generated a great deal of experience with single crystal ice, its flaws, and optical characteristics. It has been found that the characteristic growth habits whereby the c-axis is perpendicular to the boule axis, and the a-axis is perpendicular to the ice/water growth interface can be explained from the perspective of surface energies of the various faces, and a selection process. A polycrystalline seed provides a sampling of the “orientation space”, and randomly oriented grains are selected out or in of the growth process based upon orientation. In the end, only those crystals having orientation with their c-axis parallel to the ice/water growth interface (i.e.: perpendicular to the boule axis) survive the selection.

5 Appendix I

5.1 On the simplification of I_{ppp} under certain constraints

Reprinted in part with permission from: Shultz, M. J.; Bisson, P.; Groenzin, H.; Li, I. Multiplexed polarization spectroscopy: Measuring surface hyperpolarizability orientation. *J. Chem. Phys.* **2010**, *133*, 054702-054711. Copyright 2010, American Institute of Physics.

In general, a p -polarized infrared and p -polarized visible beam produces a p -polarized sum frequency:^{62-64,102}

$$\begin{aligned}
 I_{ppp} \propto & \left| \cos \eta_{r,SF} L_X \chi_{XXZ} K_X^{vis} K_Z^{IR} e_{vis}^p e_{IR}^p \right. \\
 & + \cos \eta_{r,SF} L_X \chi_{XZX} K_Z^{vis} K_X^{IR} e_{vis}^p e_{IR}^p \\
 & + \sin \eta_{r,SF} L_Z \chi_{ZXX} K_X^{vis} K_X^{IR} e_{vis}^p e_{IR}^p \\
 & \left. + \sin \eta_{r,SF} L_Z \chi_{ZZZ} K_Z^{vis} K_Z^{IR} e_{vis}^p e_{IR}^p \right|^2
 \end{aligned} \tag{5.1}$$

Note that K_Z differs from that of Shen *et al.*¹⁰³ due to application of Snell's law to assist with connection with Fresnel factors in Born and Wolf.¹⁰⁴ Let A_{ppp} be the amplitude of the ppp signal intensity, i.e. the quantity inside the absolute square in Eq. (5.1). In the case where the infrared and visible input beams are coaxial, or nearly so, and co-propagating A_{ppp} simplifies as follows. The first two subscripts of the surface hyperpolarizability, χ_{IJK} , correspond to the surface Raman tensor which, in the absence of a visible resonance, is symmetric on interchange of subscripts: $\chi_{IJK} = \chi_{JIK}$. With this equality, the sum of the middle terms is:

$$[\cos \eta_{r,SF} L_X K_Z^{vis} + \sin \eta_{r,SF} L_Z K_X^{vis}] \chi_{ZXX} K_X^{IR} e_{vis}^p e_{IR}^p \tag{5.2}$$

The index of refraction for the visible and sum frequency beams are nearly equal so the Fresnel and angle factor term, aside from common constants, is:

$$\begin{aligned} & \cos \eta_{r,SF} L_X K_Z^{vis} + \sin \eta_{r,SF} L_Z K_X^{vis} = \\ & \frac{4n_1^2 n_2 \cos \eta_{t,\omega_1} \cos \eta_{r,SF}}{(n')^2 (n_{1,SF} \cos \eta_{t,SF} + n_{2,SF} \cos \eta_{r,SF}) (n_{1,\omega_1} \cos \eta_{t,\omega_1} + n_{2,\omega_1} \cos \eta_{i,\omega_1})} \times \\ & [n_1 \sin \eta_{r,SF} \cos \eta_{t,\omega_1} - n_2 \cos \eta_{t,SF} \sin \eta_{t,\omega_1}] \end{aligned} \quad (5.3)$$

Applying Snell's law, the term in square brackets is equal to $n_2 [\sin \eta_{t,SF} \cos \eta_{t,\omega_1} - \cos \eta_{t,SF} \sin \eta_{t,\omega_1}] = \sin(\eta_{t,SF} - \eta_{t,\omega_1})$. For near coaxial, co-propagating geometry, the difference between the visible and SF angle is very small since the visible photon carries most of the momentum. The sum in equation (5.2) is thus negligible, resulting in the simplification:

$$A_{ppp} = [\cos \eta_{r,SF} L_X \chi_{XXZ} K_X^{vis} + \sin \eta_{r,SF} L_Z \chi_{ZZZ} K_Z^{vis}] K_Z^{IR} e_{vis}^p e_{IR}^p \quad (5.4)$$

This form is Eq. (1.6) in the body of the thesis.

5.2 Ice Crucible Design

Below (**Figure 5.1**) is the rough design of the ice crucible. This design was developed by Groenzin and Li^{91,92}. The diagram illustrates placement of the clamping reference line and filling depth which were developed as part of the new production control process.

The crucible itself is constructed of borosilicate glass, custom blown by a professional fabricator to our specifications. The crucible is prepared by soaking overnight in concentrated sulfuric acid enhanced with an inorganic oxidizer (NOCHROMIX[®], Godax Laboratories, Inc.). Following the sulfuric acid soak, the crucible was drained and rinsed several times with 18M ohm water. After rinsing, the crucible was soaked overnight and rinsed for three additional days. That is, three

soak/rinse cycles. After this preparation, the crucible was considered acceptable for growth.

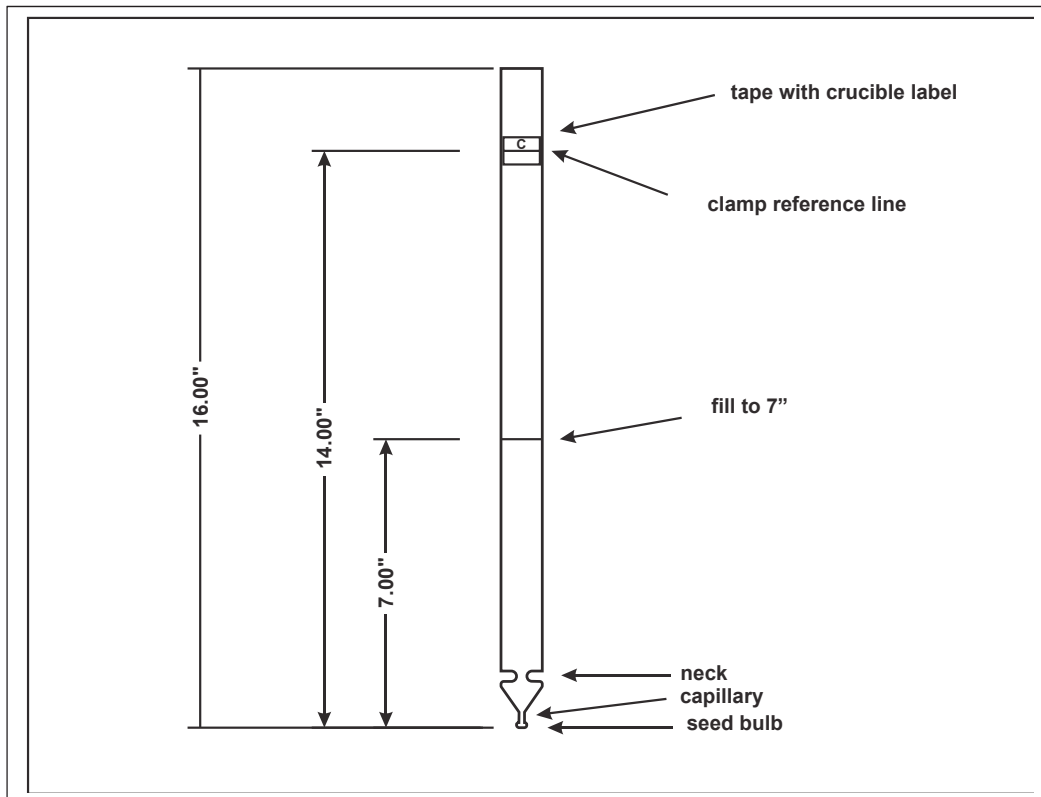


Figure 5.1 - Ice Crucible Design. In use, the crucible is filled to 7” water depth. The crucible is clamped into the drive system at the reference line near the top. Each crucible is labeled for tracking purposes. The neck, capillary, and seed bulb play a key role in the domain selection process.

5.3 Ice Cell Design

The ice cell is a basic “clam shell” with a top (the “cap”) and lower half (the “cup”). The cup is made of conventional borosilicate glass while the cap is made of fused quartz. The cap incorporates two fused quartz windows of 1.25” diameter and 0.125” thickness. The windows are tipped so as to be (approximately) perpendicular to the incoming VIS and IR beams (55°) and the outgoing SF beam (52°).

The cap and cup have flat, flame polished glass flanges that mate over double concentric O-rings. In **Figure 1.12**, the O-rings can be seen resting on the flange of the

cup. In use, the cap and top are compressed together using a ring and three screws arranged at 120 degrees around the periphery.

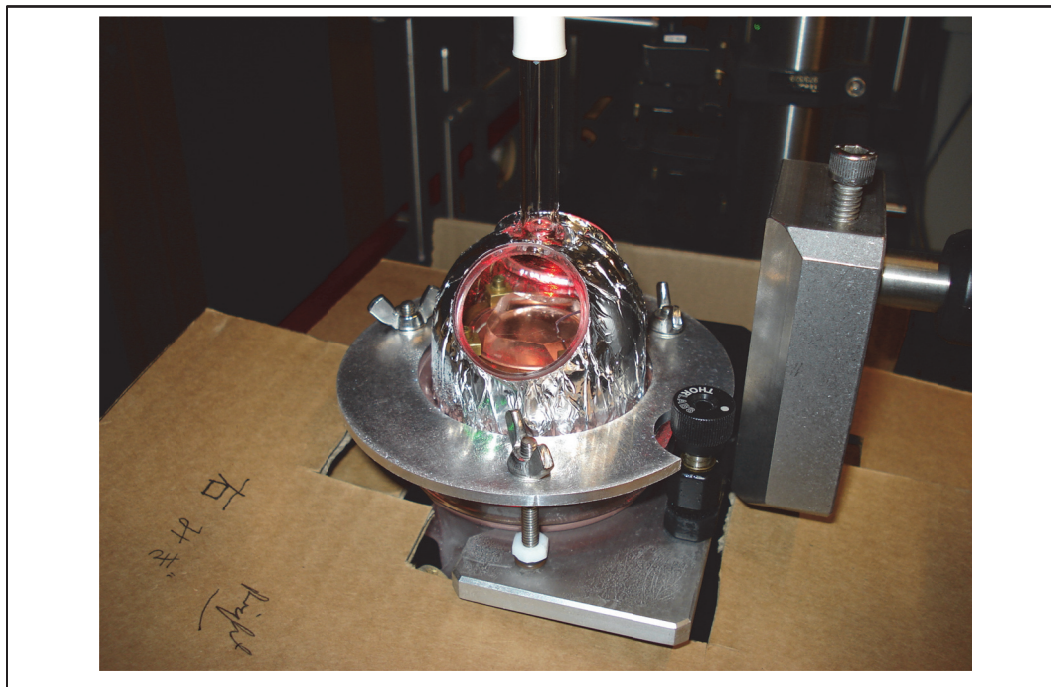


Figure 5.2 - Assembled Cell on the Bench. The perspective is looking at the “output” window. The flat clamping ring and three screws with wing-nuts compress the cap, O-rings, and cup together to make a seal. The cap has been wrapped with one layer of aluminum foil to improve thermal performance. A sample of ice can be seen inside the cell.

5.4 Heat sink design

Originally, a smooth 3/4” diameter thermal conductor was used between the ice mounting pedestal and the liquid nitrogen in the Dewar. But, early on, it was noticed that occasionally the low temperature steady state would not fall below about -125 °C. This unusual behavior was truly puzzling until several experiments were performed where the temperature vs. time profile was recorded. Some of these profiles showed an abrupt discontinuity at about -125 °C and when that occurred, the temperature at the top surface

of the ice fell to $-160\text{ }^{\circ}\text{C}$ and even to $-170\text{ }^{\circ}\text{C}$ on occasion. If the abrupt and rapid change in ice temperature didn't occur, the ice never cooled to such low temperatures.

Observing the thermal conductor carefully during the cool down, it was noted that a thin vapor barrier was present between heat sink and liquid nitrogen. It was surmised that this vapor barrier was defeating the function of the heat sink due to its low thermal conductivity. The vapor barrier is caused by the relatively "hot" copper heat sink boiling the liquid nitrogen so rapidly that the liquid nitrogen never came into direct contact with the copper. This vapor barrier caused by a hot surface against a liquid was first observed by Leidenfrost¹⁰⁵ in 1756. This is a well-known phenomenon as anyone who has dashed some water droplets on a hot frying pan can observe. When the temperature difference between the boiling point of the liquid and the hot surface is great enough, the vapor barrier will develop. When the difference falls below a certain threshold, the liquid can come into direct contact with the hot surface and a large amount of heat is transferred to the liquid. Recently, Arnaldo del Cerro¹⁰⁶ used this effect to enhance the anti-icing properties of nano-textured, hydrophobic surfaces. But, the opposite performance is required in this instance.

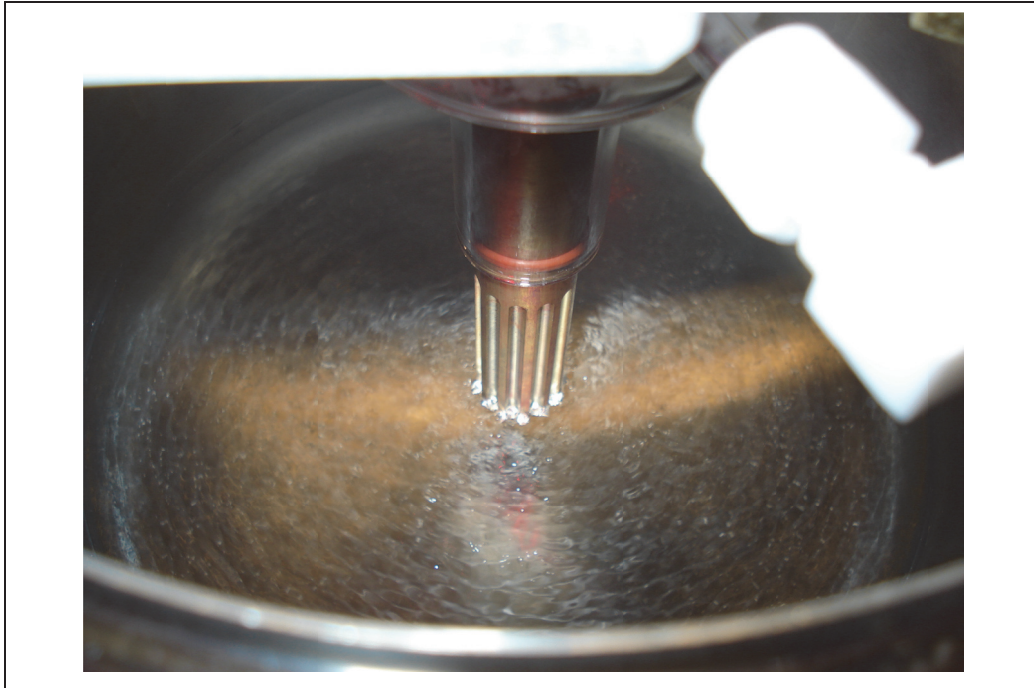


Figure 5.3 – The fluted heat sink partially immersed in the LN2. Here, the copper is fully wetted and there is no Leidenfrost vapor barrier.

The heat sink design was changed from a smooth cylinder to one where linear flutes are machined on the surface. These flutes do increase the surface area in contact with the liquid nitrogen, but that is a secondary effect. Rather, the flutes introduce sharp corners or asperities that can cool to below the Leidenfrost threshold and initiate a cascade of cooling, bringing the liquid nitrogen into direct contact with the copper. With the introduction of the fluted heat sink, ice temperatures at or below $-160\text{ }^{\circ}\text{C}$ became routine. For a view of the fluted heat sink, see **Figure 1.12** and **Figure 5.3**. The fluted heat sink can be observed at the bottom of the photographs.

5.4.1 Ice carrier

Early on, it was observed that there were some tough mechanical problems with cooling the ice sample down to cryogenic temperatures. The problems were twofold: First, the ice frequently cracked to such an extent that no single surface was large enough

to reflect the full spot of the lasers. Second, the ice frequently de-laminated from the heat sink. When this happened, good thermal conductivity was compromised, and the ice sample itself was picked up off the copper surface due to the spring force of the thermocouple attached to the top surface of the ice.

The problems of cracking and delaminating are related and result from the differences in thermal expansion coefficient. Here, the anomalous properties of ice become readily apparent. Ice has a much greater coefficient of thermal expansion than copper,⁹⁶ especially in the -20° to -100°C region. During cool down, the ice contracts much more than the copper on which it is stuck. This induces a great deal of strain that exceeds the strength of the ice.¹⁰⁷ The result is that the ice cracks within its bulk, or it shears the copper/ice interface resulting in delamination.

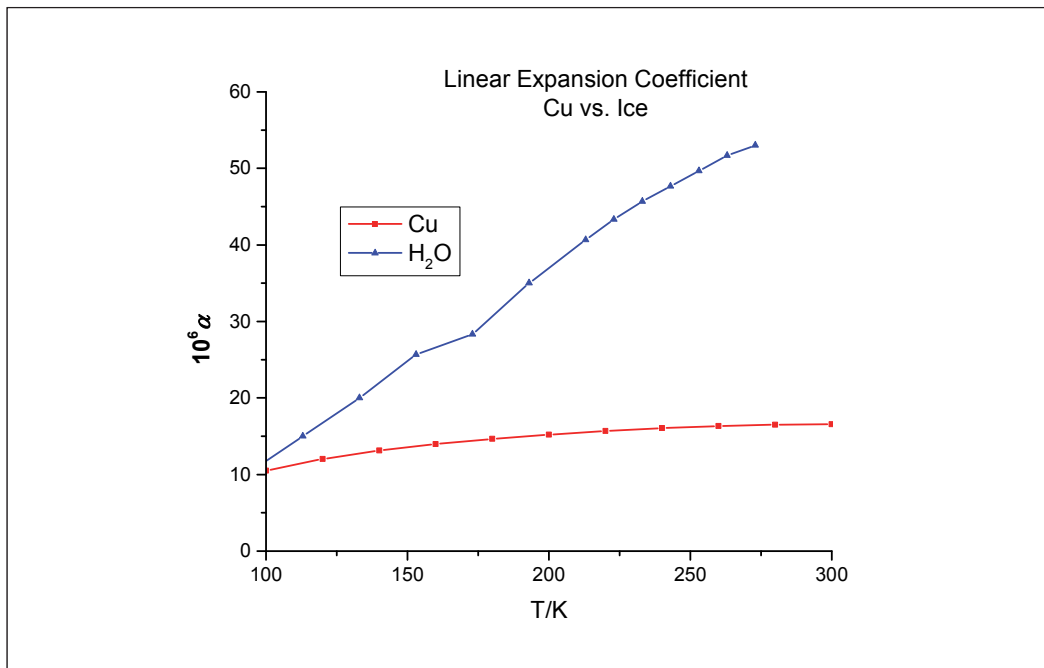


Figure 5.4 - Linear expansion of Cu vs. Ice. The greatest difference, and therefore the greatest induced strain, occurs at the warmest temperatures. Experimentally, cracking occurs at about -50°C .

It was desirable to mitigate the cracking and especially the delamination problem. So, the method of attachment of the ice to the heat sink was changed. It was felt that if the ice were attached to a thin “membrane” of copper, rather than the thick copper pedestal itself, the membrane could deform (i.e.: stretch) under the stress of the ice contracting and therefore reduce the tendency of the sample to crack or delaminate.

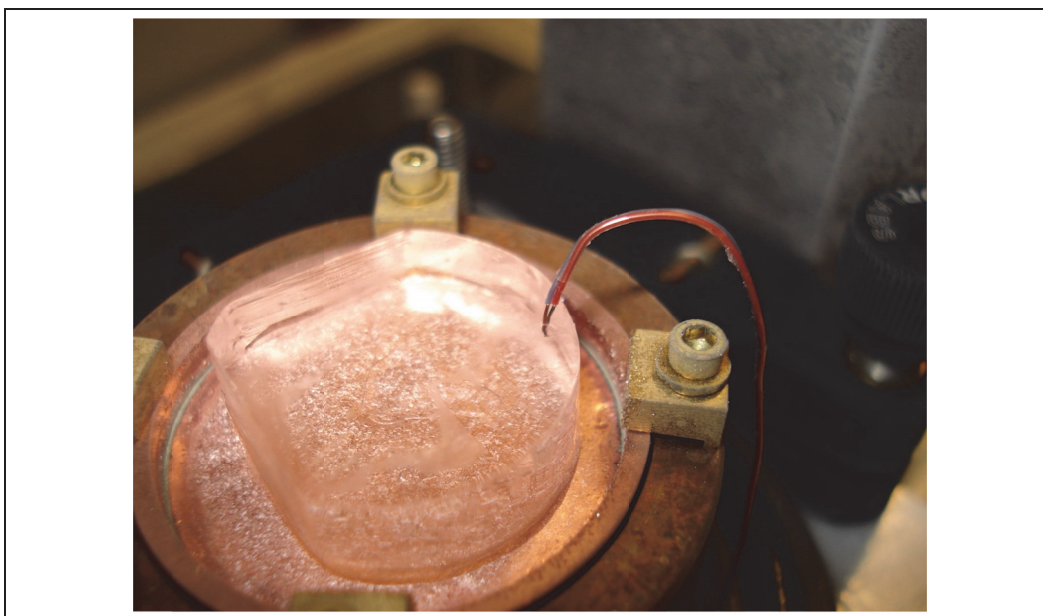


Figure 5.5 - Ice in a carrier, on the pedestal on the bench. The fused quartz top has been removed to allow this photograph. This is a prism face sample. The thermocouple, used to measure ice surface temperatures, can be seen imbedded in the top surface.

The initial design utilized a membrane composed of 0.001” thick copper foil. This design worked well in that cracking and delamination were largely suppressed, but the 0.001” thick foil was not very robust mechanically and the carrier could only be used once before it had to be re-built. As a compromise, the 0.001” thick foil was replaced with 0.002” thick foil, and this design proved to have much better resistance to wear and tear. The slightly thicker membrane also helped with better mechanical stability when the ice sample was microtomed. The thicker membrane allowed for a little more cracking,

but delamination was still effectively suppressed. In many hundreds of experiments, delamination did occur only a couple of times, and even those few times could be traced to poor fusing of the ice on to the membrane.

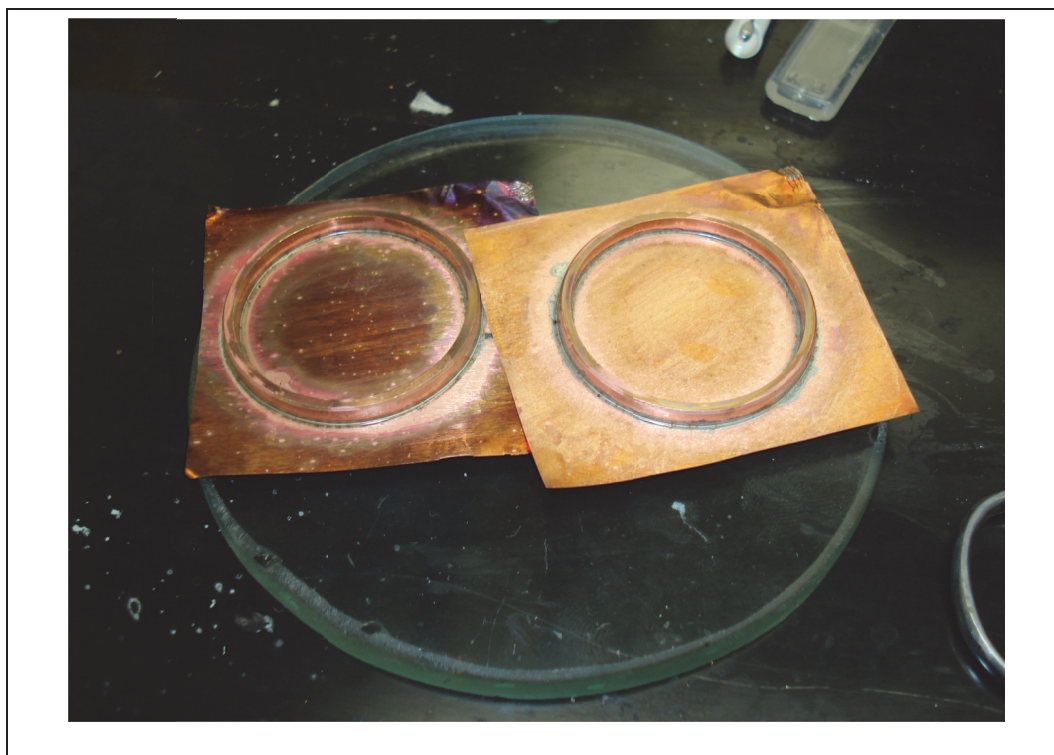


Figure 5.6 - Two carriers being fabricated. The thin 0.002" copper foil is soldered to the carrier body (ring). Afterwards, the excess is trimmed off and the completed carrier is cleaned with a sequence of organic solvents (hexanes, acetone, methanol) to remove flux residues. Following this, the carrier is slightly etched in 0.1M HNO₃ to remove copper oxides.

5.4.2 Embedding the thermocouple

As **Figure 5.5** shows, the thermocouple is actually embedded within the ice sample rather than simply “glued” to the surface using a drop of water. The ice/carrier assembly process is done in the -20 °C freezer. At that temperature, ice can be very slightly hydrophobic. If a drop of water is used to “glue” the thermocouple to the surface, it is sometimes very difficult to get the drop to properly fuse to the surface of the ice

sample. This poor adhesion often resulted in the thermocouple “popping off” the surface, or even giving inaccurate data on the true surface temperature. Even when fusing is successful, local heating around the drop damages the ice surface in a large region around the drop. Sometimes, the damage encompasses a significant portion of the area of the top surface.

It was discovered that if the thermocouple was disconnected from the meter, and an electrical current of about 1 ampere was passed through the thermocouple junction, it would become warm. After about 15 seconds of heating, the thermocouple could be plunged into the top surface of the sample. After the thermocouple was embedded into the ice, the current could be turned off and the thermocouple would freeze in place. This technique did much less damage to the top surface of the ice, reduced the potential for contamination, and was highly reliable.

5.5 Raman Spectrometer II

As mentioned in the acknowledgement section, I designed and built a second generation, compact, Raman spectrometer for use by Prof. Whitten in his teaching classroom, and also by Prof. Shultz for use in her TiO₂ research. While the original design focused on low cost, and off the shelf components, this second generation design centered on a compact footprint, and higher performance.

The design is of a classic layout where the Raman scattering is collected at right angles to the exciting laser. The samples are assumed to be liquid: a cuvette holder is built into the design. Changes in this design targeting enhanced performance are the use of 4x microscope objectives to focus the exciting laser, and also to collect the scattered Raman light. The new design now incorporates Glan-Thompson prism polarizers that have high damage thresholds, and low transmission loss as compared to the simple linear, plastic polarizers of the earlier design. A high quality optical rotation stage mounts one polarizer and can optionally be used to measure depolarization ratio. A high efficiency free-space to fiber optic coupler is used to couple the scattered Raman light into a 50 μ m, multi-mode fiber.

In common with the earlier design, the optical bench is a 1/8 m, half-Zerney-Turner monochromator with a 25 μ m slit. The detector is a linear CCD array, functioning at room temperature. That is to say, the monochromator/detector is the optical bench of an Ocean Optics USB-4000/USB-2000 miniature spectrometer system.

The excitation is supplied by a Nichia 405nm wavelength diode laser, delivering about 100mW of CW power at ca. 130 mA forward current. The diode laser is powered by a simple LM317 linear voltage regulator set up in constant current mode. The diode laser, mounting module, a-spherical collimation lens, and driver electronics are enclosed

in a small BUD box. +9VDC power is supplied by an external switching 120VAC to DC converter module. The whole spectrometer fits on an 8"x10" optical breadboard.

Figure 5.7, below shows the (partially constructed) spectrometer:

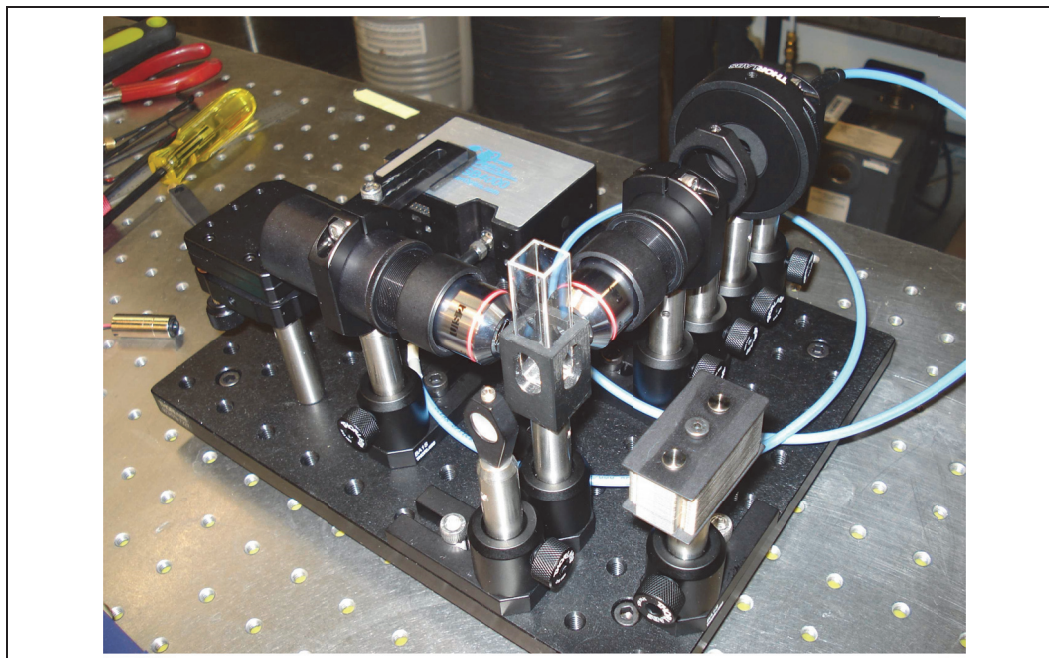


Figure 5.7 – A partly constructed Raman Spectrometer II. The laser driver/module has been removed (upper left). The excitation arm is upper left to center. The scattering arm is center to upper right. The blue fiber optic couples the scattered Raman light to the USB-4000 (top center).

Once construction was complete, a test spectrum of water was taken to verify proper operation of the instrument. **Figure 5.8**, below shows the spectrum.

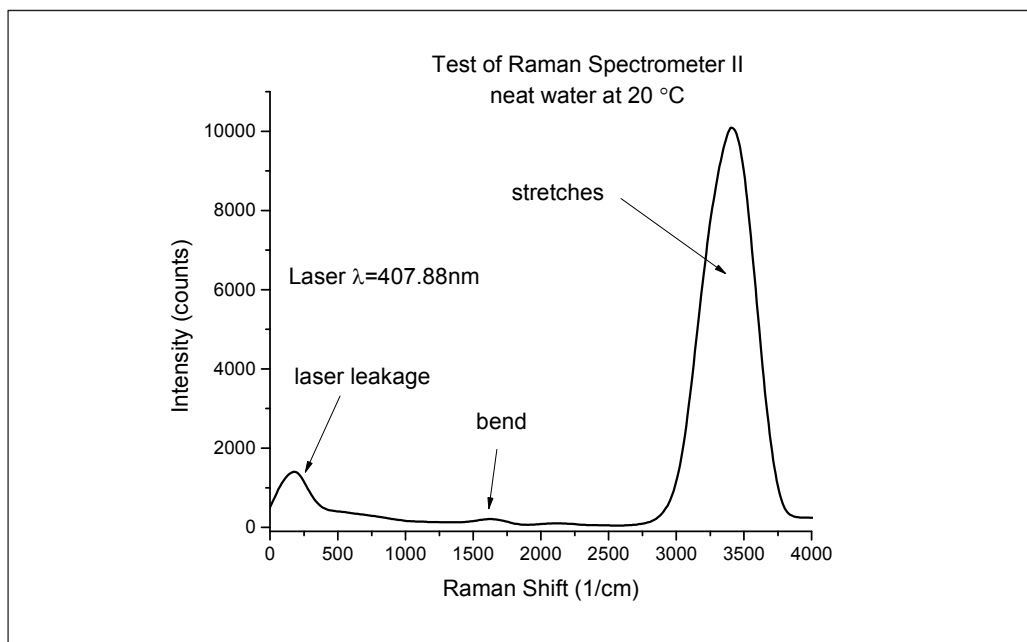


Figure 5.8 – Operational check of Raman Spectrometer II. The laser is operating a little redder than usual. The diode was later replaced with one operating closer to 405nm for a better match to the 405nm notch filter. This instrument is about twice as sensitive as the original design.

The broad peak spanning the 3000 cm^{-1} to 3800 cm^{-1} is typical of the Raman spectrum of water. The bend at 1620 cm^{-1} is often attributed to the symmetric bend and is typically very weak. For this test, the diode laser was a bit redder than desirable. At $\lambda = 407.88\text{nm}$, it was a poor match to the well centered 405nm notch filter and there was excessive laser line leakage. Subsequent to this operational check, the diode laser was replaced with one having a line ca. 404.5nm.

Bibliography

- (1) Bisson, P. J.; Whitten, J. E. Studying fast reactions: Construction and use of a low-cost continuous-flow instrument. *J. Chem. Educ.* **2006**, *83*, 1860-1863.
- (2) Patrick Bisson, G. P., Diane Rigos, James E. Whitten. Low-Cost Raman Spectroscopy using a Violet Diode Laser. *Chem. Educator [online]* **2006**, *11*, 88-92.
- (3) Cheng, M. H.; Callahan, K. M.; Margarella, A. M.; Tobias, D. J.; Hemminger, J. C.; Bluhm, H.; Krisch, M. J. Ambient Pressure X-ray Photoelectron Spectroscopy and Molecular Dynamics Simulation Studies of Liquid/Vapor Interfaces of Aqueous NaCl, RbCl, and RbBr Solutions. *J. Phys. Chem. C* **2011**, *116*, 4545-4555.
- (4) Lewis, T.; Winter, B.; Stern, A. C.; Baer, M. D.; Mundy, C. J.; Tobias, D. J.; Hemminger, J. C. Dissociation of Strong Acid Revisited: X-ray Photoelectron Spectroscopy and Molecular Dynamics Simulations of HNO₃ in Water. *J. Phys. Chem. B* **2011**, *115*, 9445-9451.
- (5) Mochida, M.; Finlayson-Pitts, B. J. FTIR Studies of the Reaction of Gaseous NO with HNO₃ on Porous Glass: Implications for Conversion of HNO₃ to Photochemically Active NO_x in the Atmosphere. *J. Phys. Chem. A* **2000**, *104*, 9705-9711.
- (6) Baltrusaitis, J.; Jayaweera, P. M.; Grassian, V. H. Sulfur Dioxide Adsorption on TiO₂ Nanoparticles: Influence of Particle Size, Coadsorbates, Sample Pretreatment, and Light on Surface Speciation and Surface Coverage. *J. Phys. Chem. C* **2010**, *115*, 492-500.

-
- (7) Rahaman, A.; Grassian, V. H.; Margulis, C. J. Dynamics of Water Adsorption onto a Calcite Surface as a Function of Relative Humidity. *J. Phys. Chem. C* **2008**, *112*, 2109-2115.
- (8) Chen, H.; Navea, J. G.; Young, M. A.; Grassian, V. H. Heterogeneous Photochemistry of Trace Atmospheric Gases with Components of Mineral Dust Aerosol. *J. Phys. Chem. A* **2011**, *115*, 490-499.
- (9) Ghosal, S.; Hemminger, J. C.; Bluhm, H.; Mun, B. S.; Hebenstreit, E. L. D.; Ketteler, G.; Ogletree, D. F.; Requejo, F. G.; Salmeron, M. Electron spectroscopy of aqueous solution interfaces reveals surface enhancement of halides. *Science* **2005**, *307*, 563-566.
- (10) Liu, J.-H.; Zhang, Y.-H.; Wang, L.-Y.; Wei, Z.-F. Drawing out the structural information of the first layer of hydrated ions: ATR-FTIR spectroscopic studies on aqueous NH_4NO_3 , NaNO_3 , and $\text{Mg}(\text{NO}_3)_2$ solutions. *Spectrochim. Act. A* **2005**, *61*, 893-899.
- (11) Shen, Y. R.; Ostroverkhov, V. Sum-frequency vibrational spectroscopy on water interfaces: Polar orientation of water molecules at interfaces. *Chem. Rev.* **2006**, *106*, 1140-1154.
- (12) Tian, C.; Ji, N.; Waychunas, G. A.; Shen, Y. R. Interfacial Structures of Acidic and Basic Aqueous Solutions. *J. Am. Chem. Soc.* **2008**, *130*, 13033-13039.
- (13) Gopalakrishnan, S.; Jungwirth, P.; Tobias, D. J.; Allen, H. C. Air-liquid interfaces of aqueous solutions containing ammonium and sulfate: Spectroscopic and molecular dynamics studies. *J. Phys. Chem. B* **2005**, *109*, 8861-8872.
- (14) Gopalakrishnan, S.; Liu, D.; Allen, H. C.; Kuo, M.; Shultz, M. J. Vibrational Spectroscopic Studies of Aqueous Interfaces: Salts, Acids, Bases, and Nanodrops. *Chem. Rev. (Washington, DC, U. S.)* **2006**, *106*, 1155-1175.

-
- (15) Walker, D. S.; Richmond, G. L. Understanding the effects of hydrogen bonding at the vapor-water interface: Vibrational sum frequency spectroscopy of H₂O/HOD/D₂O mixtures studied using molecular dynamics simulations. *J. Phys. Chem. C* **2007**, *111*, 8321-8330.
- (16) McFearin, C. L.; Richmond, G. L. The Role of Interfacial Molecular Structure in the Adsorption of Ions at the Liquid-Liquid Interface. *J. Phys. Chem. C* **2009**, *113*, 21162-21168.
- (17) Baldelli, S.; Schnitzer, C.; Shultz, M. J.; Campbell, D. J. Sum Frequency Generation Investigation of Water at the Surface of H₂O/H₂SO₄ Binary Systems. *J. Phys. Chem. B* **1997**, *101*, 10435-10441.
- (18) Hobbs, P. V. *Ice Physics*, paperback ed.; Oxford University Press, Inc.: New York, NY, 1974.
- (19) Petrenko, V. F.; Whitworth, R. W. *Physics of Ice*; Oxford University Press, Inc.: New York, NY, 1999.
- (20) Prosser, A. J.; Franses, E. I. Infrared Reflection Absorption Spectroscopy (IRRAS) of aqueous nonsurfactant salts, ionic surfactants, and mixed ionic surfactants. *Langmuir* **2002**, *18*, 9234-9242.
- (21) Roy, D.; Fendler, J. Reflection and absorption techniques for optical characterization of chemically assembled nanomaterials. *Adv. Mater.* **2004**, *16*, 479-508.
- (22) Zondlo, M. A.; Onasch, T. B.; Warshawsky, M. S.; Tolbert, M. A.; Mallick, G.; Arentz, P.; Robinson, M. S. Experimental Studies of Vapor-Deposited Water-Ice Films Using Grazing-Angle FTIR-Reflection Absorption Spectroscopy. *J. Phys. Chem. B* **1997**, *101*, 10887-10895.

-
- (23) Eftekhari-Bafrooei, A.; Nihonyanagi, S.; Borguet, E. Spectroscopy and Dynamics of the Multiple Free OH Species at an Aqueous/Hydrophobic Interface. *J. Phys. Chem. C* **2012**, *116*, 21734–21741.
- (24) Buch, V.; Tarbuck, T.; Richmond, G. L.; Groenzin, H.; Li, I.; Shultz, M. J. Sum frequency generation surface spectra of ice, water, and acid solution investigated by an exciton model. *J. Chem. Phys.* **2007**, *127*, 204710-15.
- (25) Gragson, D. E.; McCarty, B. M.; Richmond, G. L. Ordering of interfacial water molecules at the charged air/water interface observed by vibrational sum frequency generation. *J. Am. Chem. Soc.* **1997**, *119*, 6144-6152.
- (26) Allen, H. C.; Raymond, E. A.; Richmond, G. L. Non-linear vibrational sum frequency spectroscopy of atmospherically relevant molecules at aqueous solution surfaces. *Curr. Op. Coll. Interf. Sci.* **2000**, *5*, 74-80.
- (27) Moore, F. G.; Becraft, K. A.; Richmond, G. L. Challenges in interpreting vibrational sum frequency spectra: Deconvoluting spectral features as demonstrated in the calcium fluoride-water-sodium dodecylsulfate system. *App. Spec.* **2002**, *56*, 1575-1578.
- (28) Librovich, N. B.; Sakun, V. P.; Sokolov, N. D. H⁺ and OH⁻ ions in aqueous solutions vibrational spectra of hydrates. *Chem. Phys.* **1979**, *39*, 351-366.
- (29) Tian, C. S.; Shen, Y. R. Sum-frequency vibrational spectroscopic studies of water/vapor interfaces. *Chem. Phys. Lett.* **2009**, *470*, 1-6.
- (30) Bonn, M.; Bakker, H. J.; Tong, Y. J.; Backus, E. H. G. No Ice-Like Water at Aqueous Biological Interfaces. *Biointerphases* **2012**, *7*, 1-4.
- (31) Nihonyanagi, S.; Ishiyama, T.; Lee, T.; Yamaguchi, S.; Bonn, M.; Morita, A.; Tahara, T. Unified Molecular View of the Air/Water Interface Based on

-
- Experimental and Theoretical $\chi^{(2)}$ Spectra of an Isotopically Diluted Water Surface. *J. Am. Chem. Soc.* **2011**, *133*, 16875-16880.
- (32) Benderskii, V. A.; Kats, E. I. Propagating vibrational excitations in molecular chains. *J. Exp. Theo. Phys.* **2011**, *94*, 459-464.
- (33) Ghosh, A.; Smits, M.; Sovago, M.; Bredenbeck, J.; Müller, M.; Bonn, M. Ultrafast vibrational dynamics of interfacial water. *Chem. Phys.* **2008**, *350*, 23-30.
- (34) McGuire, J. A.; Shen, Y. R. Ultrafast Vibrational Dynamics at Water Interfaces. *Science* **2006**, *313*, 1945-1948.
- (35) Bordenyuk, A. N.; Benderskii, A. V. Spectrally- and time-resolved vibrational surface spectroscopy: Ultrafast hydrogen-bonding dynamics at D₂O/CaF₂ interface. *J. Chem. Phys.* **2005**, *122*, 134713-11.
- (36) Ji, N.; Ostroverkhov, V.; Chen, C.-Y.; Shen, Y.-R. Phase-Sensitive Sum-Frequency Vibrational Spectroscopy and Its Application to Studies of Interfacial Alkyl Chains. *J. Am. Chem. Soc.* **2007**, *129*, 10056-10057.
- (37) Chen, X.; Hua, W.; Huang, Z.; Allen, H. C. Interfacial Water Structure Associated with Phospholipid Membranes Studied by Phase-Sensitive Vibrational Sum Frequency Generation Spectroscopy. *J. Am. Chem. Soc.* **2010**, *132*, 11336-11342.
- (38) Sovago, M.; Vartiainen, E.; Bonn, M. Determining Absolute Molecular Orientation at Interfaces: A Phase Retrieval Approach for Sum Frequency Generation Spectroscopy. *J. Phys. Chem. C* **2009**, *113*, 6100-6106.
- (39) Wei, X.; Miranda, P. B.; Zhang, C.; Shen, Y. R. Sum-frequency spectroscopic studies of ice interfaces. *Phys. Rev. B* **2002**, *66*, 085401: 1-13.

-
- (40) Groenzin, H.; Li, I.; Shultz, M. J. Sum-frequency generation: Polarization surface spectroscopy analysis of the vibrational surface modes on the basal face of ice I_h . *J. Chem. Phys.* **2008**, *128*, 214510: 1-8.
- (41) Groenzin, H.; Li, I.; Buch, V.; Shultz, M. J. The single-crystal, basal face of ice I_h investigated with sum frequency generation. *J. Chem. Phys.* **2007**, *127*, 214502: 1 - 8.
- (42) Ishiyama, T.; Takahashi, H.; Morita, A. Origin of Vibrational Spectroscopic Response at Ice Surface. *J. Phys. Chem. Lett.* **2012**, *3*, 3001-3006.
- (43) Wei, X.; Shen, Y. R. Vibrational spectroscopy of ice interfaces. *Appl. Phys. B* **2002**, *74*, 617-620.
- (44) Wei, X.; Miranda, P. B.; Shen, Y. R. Surface vibrational spectroscopic study of surface melting of ice. *Phys. Rev. Lett.* **2001**, *86*, 1554-1557.
- (45) Buch, V.; Devlin, J. P. A new interpretation of the OH-stretch spectrum of ice. *J. Chem. Phys.* **1999**, *110*, 3437-3443.
- (46) Devlin, J. P.; Buch, V. Surface of ice as viewed from combined spectroscopic and computer modeling studies. *J. Phys. Chem.* **1995**, *99*, 16534-16548.
- (47) Bergren, M. S.; Rice, S. A. An improved analysis of the OH stretching region of the vibrational spectrum of ice I_h . *J. Chem. Phys.* **1982**, *77*, 583-602.
- (48) Ketcham, W. M.; Hobbs, P. V. An experimental determination of the surface energies of ice. *Phil. Mag.* **1969**, *19*, 1161-1173.
- (49) Ketcham, W. M.; Hobbs, P. V. The preferred orientation in the growth of ice from the melt. *J. Crys. Gr.* **1967**, *1*, 263-270.
- (50) Winterbottom, W. L. Equilibrium shape of a small particle in contact with a foreign substrate. *Act. Met.* **1967**, *15*, 303-310.
- (51) Saito, Y. Wulff polyhedra derived from morse potentials and crystal habits of bcc and fcc metal particles. *J. Crys. Gr.* **1981**, *53*, 273-279.

-
- (52) Barnard, A. S.; Zapol, P. A model for the phase stability of arbitrary nanoparticles as a function of size and shape. *J. Chem. Phys.* **2004**, *121*, 4276-4283.
- (53) Bernal, J. D.; Fowler, R. H. A Theory of Water and Ionic Solution, with Particular Reference to Hydrogen and Hydroxyl Ions. *J. Chem. Phys.* **1933**, *1*, 515-548.
- (54) Pauling, L. The Structure and Entropy of Ice and of Other Crystals with Some Randomness of Atomic Arrangement. *J. Am. Chem. Soc.* **1935**, *57*, 2680-2684.
- (55) Shultz, M. J. Sum Frequency Generation: An Introduction with Recent Developments and Current Issues. In *Advances in Multi-photon Processes and Spectroscopy*; Lin, S. H. V., A. A.; Fujimura, Y., Ed.; World Scientific: Singapore, 2008; Vol. 18; pp 133-199.
- (56) Bloembergen, N.; Pershan, P. Light Waves at the Boundary of Nonlinear Media. *Phys. Rev.* **1962**, *128*, 606-622.
- (57) Hirose, C.; Akamatsu, N.; Domen, K. Formulas for the analysis of surface sum-frequency generation spectrum by CH stretching modes of methyl and methylene groups. *J. Chem. Phys.* **1992**, *96*, 997-1004.
- (58) Superfine, R.; Huang, J. Y.; Shen, Y. R. Nonlinear optical studies of the pure liquid/vapor interface: Vibrational spectra and polar ordering. *Phys. Rev. Lett.* **1991**, *66*, 1066.
- (59) Eisenthal, K. B. Liquid Interfaces Probed by Second-Harmonic and Sum-Frequency Spectroscopy. *Chem. Rev.* **1996**, *96*, 1343-1360.
- (60) Zhu, X. D.; Suhr, H.; Shen, Y. R. Surface Vibrational Spectroscopy by Infrared-Visible Sum Frequency Generation. *Phys. Rev. B* **1987**, *35*, 3047-3050.
- (61) Shen, Y. R. Surface nonlinear optics Invited. *J. Opt. Soc. Am. B-Opt. Phys.* **2011**, *28*, A56-A66.

-
- (62) Shen, Y. R. Basic Theory of Surface Sum-Frequency Generation. *J. Phys. Chem. C* **2012**, *116*, 15505-15509.
- (63) Shen, Y. R. Correction to “Basic Theory of Surface Sum-Frequency Generation”. *J. Phys. Chem. C* **2013**, *117*, 11884-11884.
- (64) Shultz, M. J.; Bisson, P.; Groenzin, H.; Li, I. Multiplexed polarization spectroscopy: Measuring surface hyperpolarizability orientation. *J. Chem. Phys.* **2010**, *133*, 054702-054711.
- (65) Stockbarger, D. C. The Production of Large Single Crystals of Lithium Fluoride. *Rev. Sci. Instr.* **1936**, *7*, 133-136.
- (66) Rigsby, G. P. Crystal Fabric Studies on Emmons Glacier Mount Rainier, Washington. *J. Geo.* **1951**, *59*, 590-598.
- (67) Langway, C. C., Jr. *Ice fabrics and the universal stage*; Dept. of Defense Dept. of the Army Corps of Engineers: Wilmette Ill., 1958.
- (68) Higuchi, K. The etching of ice crystals. *Act. Met.* **1958**, *6*, 636-642.
- (69) Bryant, G. W.; Mason, B. J. Etch pits and dislocations in ice crystals. *Phil. Mag.* **1960**, *5*, 1221-1227.
- (70) Kuroiwa, D. H., Wayne L. “Chapter 4 - Studies of Ice Etching and Dislocation Etch Pits”; *Ice and Snow*, 1963, MIT.
- (71) Sinha, N. K. Dislocations in ice as revealed by etching. *Phil. Mag.* **1977**, *36*, 1385-1404.
- (72) Kim, J.; Chou, K. C.; Somorjai, G. A. Structure and Dynamics of Acetonitrile at the Air/Liquid Interface of Binary Solutions Studied by Infrared-Visible Sum Frequency Generation. *J. Phys. Chem. B* **2003**, *107*, 1592-1596.
- (73) Du, Q.; Superfine, R.; Freysz, E.; Shen, Y. R. Vibrational spectroscopy of water at the vapor/water interface. *Phys. Rev. Lett.* **1993**, *70*, 2313-2316.

-
- (74) Hertzberg, G. *Molecular Spectra and Molecular Structure II. Infrared and Raman Spectra of Polyatomic Molecules*; Krieger Publishing: Malabar, FL, 1991; Vol. 2.
- (75) Librovich, N. B.; Maiorov, V. D.; Vinnik, M. I. Determination of Hydration Numbers of Molecules and Ions from Overtone Bands in the IR-Spectrum of Water. *Bull. Acad. Sci. USSR Div. Chem. Sci.* **1977**, *26*, 1152-1156.
- (76) Wolfrum, K.; Graener, H.; Laubereau, A. Sum-frequency vibrational spectroscopy at the liquid--air interface of methanol. Water solutions. *Chem. Phys. Lett.* **1993**, *213*, 41-46.
- (77) Zhang, D.; Gutow, J. H.; Eisenthal, K. B. Structural phase transitions of small molecules at air/water interfaces. *J. Chem. Soc. Far. Trans.* **1996**, *92*, 539-543.
- (78) Shultz, M. J.; Schnitzer, C.; Simonelli, D.; Baldelli, S. Sum frequency generation spectroscopy of the aqueous interface. Ionic and soluble molecular solutions. *Int. Rev. Phys. Chem.* **2000**, *19*, 123-153.
- (79) Buch, V.; Sandler, P.; Sadlej, J. Simulations of H₂O solid, liquid, and clusters, with an emphasis on ferroelectric ordering transition in hexagonal ice. *J. Phys. Chem. B* **1998**, *102*, 8641-8653.
- (80) Gragson, D. E.; Richmond, G. L. Investigations of the structure and hydrogen bonding of water molecules at liquid surfaces by vibrational sum frequency spectroscopy. *J. Phys. Chem. B* **1998**, *102*, 3847-3861.
- (81) Jubb, A. M.; Hua, W.; Allen, H. C. Organization of Water and Atmospherically Relevant Ions and Solutes: Vibrational Sum Frequency Spectroscopy at the Vapor/Liquid and Liquid/Solid Interfaces. *Acc. Chem. Res.* **2012**, *45*, 110-119.
- (82) Mucha, M.; Frigato, T.; Levering, L. M.; Allen, H. C.; Tobias, D. J.; Dang, L. X.; Jungwirth, P. Unified Molecular Picture of the Surfaces of Aqueous Acid, Base, and Salt Solutions. *J. Phys. Chem. B* **2005**, *109*, 7617-7623.

-
- (83) Shultz, M. J.; Bisson, P.; Buch, V.; Groenzin, H.; Li, I. Aqueous hydrogen bonding probed with polarization and matrix isolation spectroscopy. *J. Mol. Struct.* **2010**, *972*, 51-58.
- (84) Tian, C.; Byrnes, S. J.; Han, H.-L.; Shen, Y. R. Surface Propensities of Atmospherically Relevant Ions in Salt Solutions Revealed by Phase-Sensitive Sum Frequency Vibrational Spectroscopy. *J. Phys. Chem. Lett.* **2011**, *2*, 1946-1949.
- (85) Nihonyanagi, S.; Yamaguchi, S.; Tahara, T. Direct evidence for orientational flip-flop of water molecules at charged interfaces: A heterodyne-detected vibrational sum frequency generation study. *J. Chem. Phys.* **2009**, *130*, 204704: 1-5.
- (86) Nakamoto, K.; Margoshes, M.; Rundle, R. E. Stretching Frequencies as a Function of Distances in Hydrogen Bonds. *J. Am. Chem. Soc.* **1955**, *77*, 6480-6486.
- (87) Ishiyama, T.; Morita, A. Molecular Dynamics Simulation of Sum Frequency Generation Spectra of Aqueous Sulfuric Acid Solution. *J. Phys. Chem. C* **2011**, *115*, 13704-13716.
- (88) Murphy, W. F. The rovibrational Raman spectrum of water vapour ν_1 and ν_3 . *Mol. Phys.* **1978**, *36*, 727-732.
- (89) Jaccard, C. Theoretical and Experimental Study of the Electrical Properties of Ice. *Helv. Phys. Acta* **1959**, *32*, 89-128.
- (90) Knight, C. A. A simple technique for growing large, optically "perfect" ice crystals. *J. Glac.* **1996**, *42*, 585-587.
- (91) Groenzin, H. Sum-Frequency studies of single crystalline ice I_h . Dissertation/Thesis, Tufts University, 2007.

-
- (92) Li, I. Sum Frequency Studies of Single Crystal Ice (Ih) as Related to its Lattice Orientation. Dissertation/Thesis, Tufts University, 2008.
- (93) Bridgman, P. W. Certain Physical Properties of Single Crystals of Tungsten, Antimony, Bismuth, Tellurium, Cadmium, Zinc, and Tin. *Proc. Am. Acad. Art. Sci.* **1925**, *60*, 305-383.
- (94) Jahne, B.; Heinz, G.; Dietrich, W. Measurement of the Diffusion-Coefficients of Sparingly Soluble Gases in Water. *J. Geophys. Res.-Oceans* **1987**, *92*, 10767-10776.
- (95) Himmelblau, D. M. Diffusion of Dissolved Gases in Liquids. *Chem. Rev.* **1964**, *64*, 527-550.
- (96) *CRC Handbook of Chemistry and Physics*; 94th ed.; Lide, D. R., Ed.; CRC Press: Boca Ratone, FL, 2014.
- (97) Libbrecht, K. Growth rates of the principal facets of ice between -10°C and -40°C . *J. Crys. Gr.* **2003**, *247*, 530-540.
- (98) Rozmanov, D.; Kusalik, P. G. Temperature dependence of crystal growth of hexagonal ice (Ih). *Phys. Chem. Chem. Phys.* **2011**, *13*, 15501-15511.
- (99) Pruppacher, H. R. Interpretation of Experimentally Determined Growth Rates of Ice Crystals in Supercooled Water. *J. Chem. Phys.* **1967**, *47*, 1807-1813.
- (100) Shibkov, A. A.; Zheltov, M. A.; Korolev, A. A.; Kazakov, A. A.; Leonov, A. A. Crossover from diffusion-limited to kinetics-limited growth of ice crystals. *J. Crys. Gr.* **2005**, *285*, 215-227.
- (101) Furukawa, Y.; Shimada, W. Three-dimensional pattern formation during growth of ice dendrites — its relation to universal law of dendritic growth. *J. Crys. Gr.* **1993**, *128*, 234-239.

- (102) Zhuang, X.; Miranda, P. B.; Kim, D.; Shen, Y. R. Mapping molecular orientation and conformation at interfaces by surface nonlinear optics. *Phys. Rev. B* **1999**, *59*, 12632-12640.
- (103) Wei, X.; Hong, S.-C.; Zhuang, X.; Goto, T.; Shen, Y. R. Nonlinear optical studies of liquid crystal alignment on a rubbed polyvinyl alcohol surface. *Physical Review E* **2000**, *62*, 5160-5172.
- (104) Born, M.; Wolf, E. *Principles of Optics: Electromagnetic Theory of Propagation, Interference and Diffraction of Light* 7th expanded ed.; Cambridge University Press: Cambridge, UK, 1999.
- (105) Leidenfrost, J. G. On the fixation of water in diverse fire. *International Journal of Heat and Mass Transfer* **1976**, *9*, 1153-1166.
- (106) Arnaldo Del Cerro, D.; Marin, A. G.; Romer, G. R.; Pathiraj, B.; Lohse, D.; Huis In 't Veld, A. J. Leidenfrost point reduction on micropatterned metallic surfaces. *Langmuir* **2012**, *28*, 15106-10.
- (107) Mohamed, A. M. A.; Farzaneh, M. An experimental study on the tensile properties of atmospheric ice. *Cold Regions Science and Technology* **2011**, *68*, 91-98.